Shape dependent transport of micro-particles in blood flow: from margination to adhesion

Huilin Ye[1], Zhiqiang Shen[1], and Ying Li[1,2]

[1]Department of Mechanical Engineering, University of Connecticut, 191 Auditorium Road, Unit 3139, Storrs, Connecticut 06269, United States, Email: yingli@engr.uconn.edu

[2]Institute of Materials Science, University of Connecticut , 97 North Eagleville Road, Unit 3136, Storrs,Connecticut 06269, United States

ABSTRACT

We explore the shape effect of micro-particles (MPs) on their margination behaviors in blood flow through three-dimensional numerical simulations. Eight different shapes of MPs are considered with identical volume, such as sphere, rod, cubic, disk, oblate and prolate with different aspect ratios. These MPs are immersed in the blood plasma, which is consists of suspension of RBCs. A simple shear flow is applied with moderate shear rate (200 s^{-1}). The fluid flow and immersed particles (RBCs and MPs) are solved by the Lattice Boltzmann method (LBM) and spring-lattice model, respectively. The fluid-structure interaction is coupled by immersed boundary method. Additionally, we adopt a stochastic model to capture the adhesive behavior of MPs near the vessel wall for ligand-receptor binding. Without near-wall adhesion, the spherical particle demonstrate the strongest margination in the blood flow. It can be attributed to the large collision displacement with RBCs and small migration distance in cross-stream direction under shear flow of spherical particles. Furthermore, under the influence of near-wall adhesion, the margination of different shaped MPs is examined. Interestingly, the adhesion can either promote or impede the margination behavior depending on the shapes of MPs. When the major axes of MPs is smaller than or comparative to the thickness of the cell-free layer in the flow channel, the adhesion can promote

margination of these MPs. While for MPs with large major axes, due to the near-wall adhesion effect, the reduce tumbling frequencies enable them to have enough time to interact with RBCs. In turn, the long time interaction with RBCs can drag these MPs to the central stream of blood flow, impeding their margination. However, the prolate particles demonstrate distinct behaviors. Apart from tumbling, the transition to precession of prolate particles near the vessel wall results in the enhancement of margination. Overall, the sphereical MP outperform other non-spherical MPs for its high margination propensity under the influence of near-wall adhesion and moderate shear flow rate. This study might offer theoretical guidance to design MP-based drug carriers in blood flow with high efficacy.

INTRODUCTION

The transport of particles in the flow is ubiquitous in nature and many industrial applications, such as chemical, biological, and mechanical engineering. The cross-stream migration of a particle in blood flow towards the periphery of vessel wall is well-known as margination(Firrell and Lipowsky 1989). Margination play an important role in understanding physiological phenomena and relevant diseases, such as atherosclerosis. For example, before leukocytes perform organism defense functions near inflammation sites, they should firstly marginate to the vessel wall region, adhere to vascular endothelium and transmigrate into the inflammatory tissues(Ley and Tedder 1995; Goldsmith and Spain 1984; Fedosov et al. 2012). The physical mechanisms of particles moving close to the endothelium and then adhering on the vessel wall have be extensively investigated and adopted in drug delivery system(Blanco et al. 2015; Müller et al. 2014; Müller et al. 2016; Decuzzi et al. 2005; Li et al. 2014; Li et al. 2016). These understandings can also guide the design of microfluidic devices for the removal of pathogens and separation of circulating tumor cells (Hou et al. 2010; Gossett et al. 2010; Bhagat et al. 2010; Li et al. 2015).

Up to date, the fundamental mechanism of margination remains to be completely revealed. The unique properties of blood, like the existence of a large number of red blood cells (RBCs), are considered to play major roles(Farutin and Misbah 2013). For example, when a micro-particle (MP) is injected into the blood flow, the dynamics of the MP is governed by the complex interplay

between hydrodynamic forces, near-wall lift force and adhesive interactions of ligands from MPs with receptors on endothelium. Note that the Brownian motion, which is significant in nanoscale phenomena, is not considered here due to the micro size of MP(Ramakrishnan et al. 2017; Ye et al. 2018). Based on their dynamics, the physiological properties of MPs play different roles during the margination. Size, shape, stiffness and surface functionalization of particle, namely '4S' parameters, have been extensively studied and used in the optimal design of the particle-based drug carriers in biomedical application(Decuzzi et al. 2009; Li et al. 2014; Li et al. 2016; Ye et al. 2018). For instance, Müller et al. 2014 found that micro-sized ellipsoidal particles outperformed sub-micro spherical particles for drug delivery system by employing mesoscopic hydrodynamic simulations using two- and three-dimensional models.

Among the '4S' parameters, shape effect attracts a broad attention in experimental, theoretical and numerical studies. Without physical presence of RBCs, nonspherical particle (discoidal particle in (Gentile et al. 2008) and rod particle in (Toy et al. 2011)) were found to marginate better than spherical or hemispherical particles in experiments. Under theoretical analysis, the discoidal particle exhibited the largest propensity to marginate in a linear laminar flow(Lee et al. 2009) and oblate particle was shown to adhere more effectively to the substrate comparing with spherical particle(Decuzzi and Ferrari 2006). While in blood flow, RBCs occupy the most space of the blood vessel. The volume fraction of RBCs is about $20 \sim 45\%$ in the normal human vasculature. The interaction between MPs and RBCs is unavoidable when MPs present in the blood vessel. It was found that, presence of RBCs can lead to 50% higher binding rate for nanoparticles to vessel wall comparing with the case without RBCs. Such a higher binding rate was associated with high dispersion and margination of nanoparticles due to the tumbling motion of RBCs(Tan et al. 2012). Further mathematical model proposed by Tokarev et al. 2011 revealed the complex characteristics of platelet margination, which was induced by the frequency of near-wall rebounding collisions between platelets and RBCs. Also, starting from advection-diffusion equations considering the RBC-RBC collision, RBC-particle collision, and particle-particle collision, Qi and Shaqfeh 2017 presented the important roles of RBC deformability and

hydrodynamic interaction in the accumulation of particle in near-wall region.

Nevertheless, local physiological environment of the blood flow varies from site to site. The shear rate, hematocrit, and diameter of the vessel are not the same. Therefore, there is no consensus on the influence of particle shape on their margination process. In the *in vivo* experiment(Decuzzi et al. 2010), the discoidal particles were observed to accumulate more than others in most of the organs. While in the liver, the cylindrical particles outperformed the others. Furthermore, the shear rate ranges from tens in large veins to thousands in arterioles(Papaioannou and Stefanadis 2005). MPs should demonstrate different behaviors in these vasculatures. (Thompson et al. 2013) found that the margination and adhesion of MPs performs differently when varying the shear rate and flow conditions (pulsatile flow and recirculation flow). In the low shear rate (200 s^{-1}), there was no obvious difference among spherical and ellipsoidal particles. While under the high shear rate (500 and 1000 s^{-1}), the ellipsoidal particles exhibited high binding rate to vessel wall than spherical ones. When considering the transport of MPs near the tumor sites, a relatively low shear rate ($\sim$ 100 s^{-1}) should be considered(Lee et al. 2009). Therefore, in present work, a fixed shear rate 200 s^{-1} is employed. The margination of MPs should be different from previous works performed under a high shear rate(Vahidkhah and Bagchi 2015; Vahidkhah et al. 2014; Decuzzi et al. 2010; Zhao and Shaqfeh 2011; Zhao et al. 2012).

Generally speaking, margination is regarded as the precondition of the near-wall adhesion(Müller et al. 2016). While adhesion may, in turn, affect the margination process. Usually margination is quantified by the number of particles moving into the cell-free layer (CFL), a thin layer near blood vessel wall without presence of RBCs(Fåhræus and Lindqvist 1931). The thickness of the CFL is typically about 2.0 $\sim$ 4.5 μm (Fedosov et al. 2010b). Micro size particle outperforms nano size one during the margination process(Lee et al. 2013). Thus, the optimal size of particles in margination can be comparable to the thickness of CFL. When particle moves near the CFl, there exists a chance for particle to interact with the vessel wall through ligand-receptor binding or non-specific interactions. Thus, adhesion should play an important role during the margination of MPs. However, this margination to adhesion process rarely attracts attention in the past(Müller

et al. 2016). Researchers pay more attention to either margination or adhesion of particles in the blood flow (Vahidkhah and Bagchi 2015; Decuzzi and Ferrari 2006; Müller et al. 2014), not the whole process.

Considering the above aspect, present study focus on shape dependent transport of MPs in blood flow, by simultaneously considering the margination and adhesion. Eight different shapes of MPs are considered with identical volume, such as sphere, rod, cubic, disk, oblate and prolate with different aspect ratios. The diameter of spherical MP is 2 μm and its volume is about 4.18 μm^3. We combine Lattice Boltzmann Method and molecular dynamics method to solve fluid dynamics and particles (RBCs and MPs) motions, respectively. Immersed boundary (IB) method is used to couple them together for fluid-structure interaction (FSI). IB method is firstly proposed by Peskin(Peskin 1972) to study the flow pattern of blood in the heart. Afterwards, it is further developed to simulate deformable objects immersed in the fluid flow (Peskin 2002; Krüger et al. 2011; Feng and Michaelides 2004; Ye et al. 2017d). IB method is widely used due to its simplicity in handling the FSI problem. IB method was a novel numerical scheme that the entire simulation of the fluid flow was carried out on an Eulerian grid, which did not conform to the shape of Lagrangian objects immersed in the flow(Mittal and Iaccarino 2005). Thus, comparing with another approach, namely the Arbitrary-Lagrangian-Eulerian method (ALE) which is also widely used to model fluid-structure interactions(Donea et al. 1982; Hughes et al. 1981; Belytschko et al. 2013), IB method can save the expensive computational cost used in the complex mesh generation as well as the procedure to project solution onto newly generated grids. The primary advantage of the IB method is that the grid generation has been greatly simplified. Generating body-conformal structured or unstructured grid is very difficult before conducting simulation of the FSI. It needs to on one side provide adequate local resolution, on the other hand expect minimum number of total grid points. These conflicting requirements result in poor grid quality, which negatively impact the accuracy and computation cost of the simulation(Ferziger and Peric 2012). Here IB method can be considered as an interface between two independent solvers: fluid solver and solid solver. These two solvers are decoupled due to the existence of IB method. Flow part is conducted on the

Eulerian grids and solid part is carried out on Lagrangian grid. This results in a high degree of versatility to develop and implement various functions involving in the FSI (Mittal and Iaccarino 2005; Peskin 2002).

Additionally, we adopt a probabilistic model proposed by (Hammer and Lauffenburger 1987) to represent the ligand-receptor binding process. First, the margination behavior of different shaped MPs is investigated and used as a reference to explore the adhesion effect. We find that spherical particle stands out due to its large collision displacement with RBCs and small shear stress induced lateral migration to central stream. Afterwards, the margination behaviors of different shaped MPs under influence of near-wall adhesion are obtained. Interestingly, the adhesion can either promote or impede the margination behavior depending on the shapes of MPs. When the major axes of MPs is smaller than or comparative to the thickness of the CFL, the adhesion can promote margination of these MPs. While for MPs with large major axes, due to the near-wall adhesion effect, the reduce tumbling frequencies enable them to have enough time to interact with RBCs. In turn, the long time interaction with RBCs can drag these MPs to the central stream of blood flow, impeding their margination. However, the prolate particles demonstrate distinct behaviors. Apart from tumbling, the transition to precession of prolate particles near the vessel wall results in the enhancement of margination.

This paper is organized as follows. Section 2 identifies the physical problem of MP transport in blood flow and describes numerical methods to solve fluid flow, particle dynamics and adhesion dynamics. Section 4 presents the margination and adhesion results, with a detailed discussion on their physical mechanisms. A short summary in Section 5 concludes this work.

COMPUTATIONAL MODEL AND METHOD

Physical problem of MP margination and adhesion

The MPs with encapsulated drug molecules are usually intravenously administrated into blood vessel and circulate with the blood flow. During this process, they may laterally migrate in the cross-stream direction, either moving to vessel wall or center of the vessel. This process is affected by collision with RBCs and shear stress exerted by the fluid flow. In the blood flow, most space

of the vessel is occupied by a large number of RBCs. In the normal human blood vasculature, the volume fraction (hematocrit Ht) of RBCs is about 20 $\sim$ 45% (Nadler et al. 1962). Therefore, the MPs can collide very frequently with RBCs. Together with the influence of shear flow, MPs may marginate from the central stream of blood to the region near the vessel wall (c.f.figure 1b).

A thin layer near vessel wall without RBCs, namely cell-free layer (CFL), can be formed due to the deformability of RBCs. The formation of CFL plays a critical role as lubricant layer and reduces the blood flow resistance, which is also called Fahraeus-Lindqvist effect (Fåhræus and Lindqvist 1931). If the MP moves into CFL, the ligands decorated on its surface will have the chance to be captured by the receptors expressed on the endothelial cell from the vessel wall (figure 1a). However, reaching CFL is not the precondition for this ligand-receptor binding. Only when the MP is within a specific distance from the vessel wall, its ligands can interact with receptors. This distance is determined by the reaction distance between ligands and receptors. Here we name the thin layer within this distance as an adhesion layer (χ). The thickness of the adhesion layer is usually about tens to hundreds nanometers (Decuzzi and Ferrari 2006; Müller et al. 2014; Müller et al. 2016). Here, we set it to be 800 nm, according to the reaction distance used in the ligand-receptor binding model. It is a reasonable choice comparing with previous work of Müller et al. 2014.

The shape effect of MPs on their margination and adhesion is investigated systemically through numerical simulations. We adopt a rectangular channel of height 36 μm, width 27 μm and length 54 μm to model the vessel. Periodical boundary conditions are applied along width (x) and length (y) directions. Height (z) direction is bounded by two flat plates. The bottom plate represents the vessel wall, also namely substrate. It is fixed while the upper one is moving with a constant velocity U to generate a simple shear flow. The major focus of this work is the shape effect of MPs on their margination and adhesion. Thus in all simulations, the shear rate is fixed to be 200 s^{-1}. There are 162 RBCs and 80 identical MPs placed inside the channel. The hematocrit (volume fraction of RBCs) is about 30%. The particle shapes are given in figure 2, such as sphere, rod, cubic, disk, oblate and prolate with different aspect ratios. They have the same volume as the spherical particle with radius 1 μm. The volume fraction of MPs in blood flow is about 0.64%. The details are

provided in Table 1 for size and shape of RBCs and MPs. In this table, the aspect ratio (AR) of nonspherical partice represents the ratio of its major axis to minor axis. On the surfaces of MPs and substrate, the ligands and receptors are uniformly distributed, respectively. The densities of ligands and receptors are also given in Table. 4.

Lattice Boltzmann Method for fluid flow

Here, the minor components of blood, such as white blood cells and platelets, are not considered due to their low volume fractions ($\sim 1\%$). The blood flow is considered as a suspension of RBCs, which are immersed in the Newtonian fluid. The dynamics of the fluid flow is governed by the Navier-Stokes equation and the continuity equation in an Eulerian coordinate system as follows:

$$\frac{\partial \mathbf{v}}{\partial t} + \mathbf{v} \cdot \nabla \mathbf{v} = -\frac{1}{\rho}\nabla p + \frac{\mu}{\rho}\nabla^2 \mathbf{v} + \mathbf{F}, \tag{1}$$

$$\nabla \cdot \mathbf{v} = 0, \tag{2}$$

where ρ, $\mathbf{v}$, p are the fluid density, velocity, and pressure, respectively. μ is the dynamic viscosity of the fluid (plasma), and $\mathbf{F}$ is the body force. Lattice Boltzmann method (LBM), which is an efficient and accurate method for Newtonian flow (Chen and Doolen 1998), is employed to solve Navier-Stokes equations. The linearized Boltzmann equation has the following form as:

$$(\partial_t + e_{i\alpha}\partial_\alpha) f_i = -\frac{1}{\tau}(f_i - f_i^{eq}) + F_i, \tag{3}$$

where $f_i(\mathbf{x}, t)$ is the distribution function for fluid particles with velocity $\mathbf{e}_i$ at position $\mathbf{x}$ and time t. $f_i^{eq}(\mathbf{x}, t)$ is the equilibrium distribution function and τ is the non-dimensional relaxation time. F_i is an external forcing term. In this simulation scheme, D3Q19 model is used (Mackay et al. 2013), and the fluid particles have possible discrete velocities stated by Mackay et al. 2013. The equilibrium distribution function $f_i^{eq}(\mathbf{x}, t)$ can be calculated as:

$$f_i^{eq}(\mathbf{x},t) = \omega_i \rho \left[1 + \frac{\mathbf{e}_i \cdot \mathbf{v}}{c_s^2} + \frac{(\mathbf{e}_i \cdot \mathbf{v})^2}{2c_s^4} - \frac{(\mathbf{v})^2}{2c_s^2}\right], \tag{4}$$

where the weighting coefficients $\omega_i = 1/3\ (i = 0), \omega_i = 1/18\ (i = 1-6), \omega_i = 1/36\ (i = 7-18)$. The term c_s represents the sound speed which equals $\Delta x/(\sqrt{3}\Delta t)$. The relaxation time is related to the kinematic viscosity in Navier-Stokes equation in the form of

$$\nu = (\tau - \frac{1}{2})c_s^2 \Delta t. \tag{5}$$

The external forcing term can be discretized by using this form (Guo et al. 2002):

$$F_i = (1 - \frac{1}{2\tau})\omega_i \left[\frac{\mathbf{e}_i - \mathbf{v}}{c_s^2} + \frac{(\mathbf{e}_i \cdot \mathbf{v})}{c_s^4}\mathbf{e}_i\right] \cdot \mathbf{F}. \tag{6}$$

Eq. (3) is solved by the algorithm proposed by (Ollila et al. 2011).

Once the particle density distribution is known, the fluid density and momentum are calculated as

$$\rho = \sum_i f_i,\ \ \rho\mathbf{v} = \sum_i f_i \mathbf{e}_i + \frac{1}{2}\mathbf{F}\Delta t. \tag{7}$$

Lattice-spring model for RBC and MP

Large-scale Atomic/Molecular Massively Parallel Simulator (LAMMPS), which is a highly parallelized tool for molecular dynamics simulations (Plimpton 1995) is adopted to capture the dynamics and deformation of deformable RBCs and rigid MPs. The RBCs are represented as liquid-filled elastic capsules with biconcave resting shape. It is modeled as a coarse-grained membrane, and the membrane is discretized to triangular elements, as given in figure 2 I, with details listed in Table. 1. The mechanical behaviors of RBC are captured by the potential function:

$$U(\{\mathbf{x}_i\}) = U_{stretching} + U_{bending} + U_{area} + U_{volume}, \tag{8}$$

where $U_{stretching}$ represents the in-plane shear resistance of membrane to deformation. $U_{bending}$

denotes the bending resistance of the lipid bilayer. U_{area} and U_{volume} are used to ensure the total area and volume conservation, corresponding to the area incompressibility of the lipid bilayer and incompressibility of the inner cytosol, respectively (Fedosov et al. 2010a; Fedosov et al. 2011b). The stretching potential $U_{stretching}$ is consisted of two parts: attractive nonlinear spring potential - wormlike chain model (WLC) and repulsive power potential - power function (POW). They are expressed as:

$$U_{WLC} = \frac{k_B T l_m}{4p} \frac{3x^2 - 2x^3}{1 - x}, \; U_{POW} = \frac{k_p}{l}, \tag{9}$$

where k_B is the Boltzmann constant and T is the temperature. $x = l/l_m \in (0, 1)$, l is the length of the spring and l_m is the maximum spring extension. p is the persistent length, and k_p is the POW force coefficient. To ensure the conservation of total area of the particle, local and global area constraints are applied. They are expressed as:

$$U_{area} = \sum_{k=1...N_t} \frac{k_d (A_k - A_{k0})^2}{2A_{k0}} + \frac{k_a (A_t - A_{t0})^2}{2A_t}, \tag{10}$$

where the first term represents the local area constraint, A_k and A_{k0} denote the area of k-th element and its initial area, respectively, and k_d is the corresponding spring constant. In the following, subscript 0 represents the corresponding initial value. The second term is the global area constraint. A_t is the total area, and k_a is the spring constant. The total volume constraint is also imposed by a harmonic potential:

$$U_{volume} = \frac{k_v (V - V_0)}{2V_0}, \tag{11}$$

where k_v is the spring constant. V is total volume. The bending potential has the form:

$$U_{bending} = \sum_{k \in 1...N_s} k_b [1 - \cos(\theta_k - \theta_0)], \tag{12}$$

where k_b is the bending stiffness. θ_k is dihedral angle between two adjacent triangular elements,

and N_s denotes the total number of dihedral angles.

The parameters used in our simulations for the RBC model are listed in Table. 2. And we apply the same model to simulate the rigid MPs. To preserve the shape of these MPs, the shear modulus of MP is set much larger than that of RBC. Additionally, we set the initial volume 2% larger than the original volume of the MP to make it initially inflated. Thus the external force like shear stress can hardly deform it. The coefficients in the potential function for MPs are also provided in Table. 3.

The accuracy of this lattice-spring model for RBC and rigid MPs has been validated in our previous works (Ye et al. 2017c; Ye et al. 2017b). In addition to above potentials, it is necessary to employ inter-molecular interactions between RBCs to represent their interactions. Here we use the Morse potential for these interactions (Liu and Liu 2006; Fedosov et al. 2011b; Tan et al. 2012), with functional form

$$U_{morse} = D_0[e^{-2\beta(r-r_0)} - 2e^{-\beta(r-r_0)}], r < r_c, \tag{13}$$

where D_0 represents the energy well depth and β controls the width of potential well. r is the distance between two particles and r_0 is the equilibrium distance. r_c is the cutoff distance. Additionally, a short range and pure repulsive Lennard-Jones potential is applied to prevent the overlapping between RBCs and MPs:

$$\mathrm{U_{LJ}}(r) = 4\epsilon[(\frac{\sigma}{r})^{12} - (\frac{\sigma}{r})^{6}], r < r_{\mathrm{LJ}}, \tag{14}$$

where ϵ is the depth of potential well. σ is the finite distance at where the LJ potential is zero. r_{LJ} is the cut-off distance. Here $r_{\mathrm{LJ}} = 2^{1/6}\sigma$ for a short range pure repulsion, which will not influence the attraction between RBCs from Morse potential. Then we set the parameters for LJ potential as $\epsilon = 1\ k_{\mathrm{B}}T, \sigma = 0.5\ \mu m$ and $r_{\mathrm{LJ}} = 0.56\ \mu m$.

Immersed boundary method for fluid-structure interaction

To account for the existence of suspended structures (i.e. RBCs or MPs) in the blood flow, the mechanical information should be transferred between fluid and structures across their boundaries.

Here, the IB method is used to couple the fluid and structure solvers. After IB was proposed by Peskin(Peskin 1972) to investigate heart valve motion in the blood flow, it was further developed to study objects such as rigid particles(Feng and Michaelides 2004), membrane(Ye et al. 2016) and other deformable particles(Krüger et al. 2011) immersed in the flow environment. Here, we adopt the original form of IB presented in Peskin(Peskin 2002) in which the detailed theoretical derivation is demonstrated. The fluid domain is represented by Eulerian coordinates $\mathbf{x}$, while the boundary of RBCs or MPs is represented by Lagrangian coordinates $\mathbf{s}$. Any position on the RBC membrane or MPs can be written as $\mathbf{X}(\mathbf{s}, t)$. The Eulerian mesh is uniform and the resolution is $\Delta x = 250\ nm$ in all directions. The Lagrangian mesh for RBC or MP is created by MATLAB (Persson and Strang 2004; Persson 2005). The mesh is approximately uniform and the size is about $\Delta X = 0.6 \sim 0.8\Delta x$. There are about 32 Eulerian points across major axis of one RBC. This is accurate enough to capture the deformation and motion of RBCs in the fluid flow (MacMECCAN et al. 2009; Vahidkhah and Bagchi 2015). $\mathbf{F}(\mathbf{s}, t)$ represents the membrane force density induced by RBC (or MP) deformation, and $\mathbf{f}(\mathbf{x}, t)$ denotes the fluid body force density. figure 3 shows the schematic of interpolation from the immersed boundary method for the fluid-structure interaction.

To satisfy the no-slip boundary condition between RBC (or MPs) and fluid flow, the flexible membrane vertices (denoted as red solid circle) should move at the same velocity as the fluid around it (green solid squares). That is

$$\frac{\partial \mathbf{X}(\mathbf{s}, t)}{\partial t} = \mathbf{u}(\mathbf{X}(\mathbf{s}, t)). \tag{15}$$

This condition will cause the membrane to deform. The membrane force density $\mathbf{F}(\mathbf{s}, t)$ is obtained by the potential functions discussed in above section, and is distributed to the surrounding fluid mesh points by

$$\mathbf{f}^{\mathrm{FSI}}(\mathbf{x}, t) = \int_{\Omega^s} \mathbf{F}^{\mathrm{FSI}}(\mathbf{X}^s, t)\delta(\mathbf{x} - \mathbf{x}^s(\mathbf{X}^s, t))d\Omega, \tag{16}$$

where δ is a smoothed approximation of the Dirac-Delta function. It should be noted that $\mathbf{F}^{\mathrm{FSI}}$ is

an area force density, while $\mathbf{f}^{\mathrm{FSI}}$ is a volumetric force density. Figure 3 shows a simple interpolation template. For simplicity, we use two-points template to illustrate the interpolation process. However, in the present 3D study, four-points interpolation template is adopted, and it is chosen to be:

$$\delta(\mathbf{x} - \mathbf{x}^s(\mathbf{X}^s, t)) = \delta(x - x(\mathbf{X}^s, t))\delta(y - y(\mathbf{X}^s, t))\delta(z - z(\mathbf{X}^s, t)), \tag{17}$$

where

$$\delta(r) = \begin{cases} \frac{1}{4}(1 + \cos(\frac{\pi|r|}{2})), & r \leq 2 \\ 0, & r > 2 \end{cases} \tag{18}$$

Then the interpolated fluid-structure interaction force is added back to the Lattice Boltzmann solver as a body force and discretized using the form Eq. (6). The accuracy of this scheme depends on the construction of delta function. Here, Eq. (18) is only the first order when sharp interfaces are simulated. The same approximation function is used to obtain the velocities of the Lagrangian nodes (RBCs or MPs) on the moving boundary. The mathematical form can be written as follows:

$$\mathbf{u}^s(\mathbf{X}^s, t) = \int_\Omega \mathbf{u}(\mathbf{x}, t)\delta(\mathbf{x} - \mathbf{x}^s(\mathbf{X}^s, t))d\Omega. \tag{19}$$

Adhesive model for ligand-receptor binding

Here, we adopt a probabilistic adhesion model to capture the formation and dissociation of biological bonds between receptors and ligands. Figure 1(a) shows the schematic of this adhesion model. When ligands on the surface of MPs are close to receptors on the vessel wall within a characteristic length d_{on}, there is a probability P_{on} to create a biological bond. Reversely, existing bond suffers a breakup probability P_{off} within a critical length d_{off}. They are defined as:

$$P_{\mathrm{on}} = \begin{cases} 1 - e^{-k_{on}\Delta t}, & l < d_{on} \\ 0, & l \geq d_{on} \end{cases}, \quad P_{\mathrm{off}} = \begin{cases} 1 - e^{-k_{off}\Delta t}, & l < d_{off} \\ 0, & l \geq d_{off} \end{cases}, \tag{20}$$

where Δt is the time step in simulation, and k_{on} and k_{off} are the association and dissociation

rates, respectively. They are defined as:

$$k_{on} = k_{on}^{0} exp(-\frac{\sigma_{on}(l-l_0)^2}{2k_BT}), \quad k_{off} = k_{off}^{0} exp(-\frac{\sigma_{off}(l-l_0)^2}{2k_BT}), \tag{21}$$

where σ_{on} and σ_{off} are the effective on and off strengths, denoting a decrease and increase of the corresponding rates within the interaction length d_{on} and d_{off}, respectively. k_{on}^{0} and k_{off}^{0} are the reaction rates at the equilibrium bond length $l = l_0$ between ligand and receptor, respectively. l_0 represents the equilibrium length of the harmonic spring, which is used to model the biological bond. Thus, the force exerted on the receptor and ligand due to existing bond is: $F_b = k_s(l - l_0)$. This adhesive model has been confirmed by our previous study (Ye et al. 2017a), and the parameters in adhesion model are chosen based on previous work of (Fedosov 2010) and (Fedosov et al. 2011a), and listed in Table. 4.

VALIDATION OF NUMERICAL METHOD

To validate the accuracy of our numerical framework, the stretching simulation of a single RBC is firstly performed to confirm the coarse-grained model of RBC. Here we compare our results with the experimental data from RBC deformation by optical tweezers(Suresh et al. 2015). We apply the uniaxial stretching force along x-direction. Figure 4(a) shows the typical configurations of the stretched RBC with stretching force 0, 68 and 100 pN. Qualitative consistence with experimental results(Suresh et al. 2015) is obtained. Furthermore, we calculate the deformation parameters such as D_A and D_T, which are the largest diameters of RBC along the stretching and transverse directions, respectively. In figure 4(b), the simulation results of D_A and D_T as functions of stretching force from 0 to 200 pN are presented. These simulation results are compared with the experimental data(Suresh et al. 2015) and previous numerical results(Fedosov et al. 2010a). We find excellent agreement between our simulation results with previous experimental and numerical results. It further confirms that our numerical model and method can accurately reproduce the mechanical behavior of a single RBC.

Then we place the RBC into the flow environment to validate the IB scheme. Figure 5(a)

shows a schematic of the RBC in shear flow driven by moving of the upper and bottom plates with same velocity but opposite directions. Figure 5(b) presents the simulation results of frequency for tumbling and tank-treading as a function of shear rate, in comparison with experimental data(Fischer 2004; Fischer 2007) and previous numerical results(Fedosov et al. 2010a). The frequency increases with the increment of shear rate in both tumbling and tank-treading regimes. Additionally, we also find an intermittent regime, in which the tumbling and tank-treading motions coexist. It is highlighted in the Figure 5(b). In this regime, the RBC initially tumbles like a solid body, and as simulation time progresses, its motion transits into tank-treading mode. The frequency in the tumbling regime is consistent with the experimental and numerical results. However, it should be emphasized that there is an obvious discrepancy between present results and the experimental data. We believe that this difference is induced by the viscosity contrast between the interior fluid of RBC and its surrounding fluid. Specifically, we compare present results with the numerical results by Fedosov *et al.*(Fedosov et al. 2010a) under the same situation. We find that they are in good agreement. Therefore, for simplicity, the viscosity contrast is set to be unity and it is confirmed to be accurate enough to capture the dynamics of RBCs in shear flow.

Additionally, the grid independence studies of fluid domain and RBC membrane are conducted. We perform a case study that a single RBC with diameter (D_r) moves in the simple shear flow shown in figure 6(a). Here the RBC is discretized with different vertexes presented in figure 6(b). First, we vary the mesh size Δx of the fluid, and track the trajectories of the RBC center along height direction (z-direction). Figure 6(c) shows that when the mesh is coarse ($\Delta x = 1/8D_r$), the trajectory is obvious different from those with fine meshes, and it is not smooth. Further increase of mesh resolution ($\Delta x = 1/16D_r$) leads to a more consistent trajectory, and only small difference exists. When the mesh resolution increases to $\Delta x = 1/32D_r$, the difference is negligible. Thus, we adopt the mesh size $\Delta x = 1/32D_r$. Furthermore, we change the discretized vertexes of the RBC membrane. Four cases $V = 766, 1418, 3286$ and 9864 are investigated here. Also, we track the trajectory of the RBC center along the height direction. We find that the discretization of the membrane has weak effect on the motion of RBC under current scheme ($766 < V < 9864$). There

is only small difference for the case of $V = 766$. To ensure enough convergence of mesh for RBC membrane, we adopt a relatively fine mesh $V = 3286$. In the following simulations, the mesh size is $\Delta x = 1/32 D_r$ and the discretization of RBC membrane is $V = 3286$.

RESULTS AND DISCUSSION

The margination of MPs with different shapes are examined (i) without and (ii) with adhesion effect. At the beginning of simulations, MPs are randomly placed with RBCs in the flow channel. However, the initial configurations for different shaped MPs may have a little difference. It is difficult to control the location of each MPs when placing them among RBCs. Nevertheless, the initial configuration effect should be negligible due to the extremely low volume fraction of MPs (less than 1%).

Margination of MPs without adhesion

Margination behavior of rigid MPs with different shapes is firstly investigated. The snapshots given in figure 7 show the margination process of spherical MP from central stream of blood flow to CFL. The spherical MPs gradually accumulate at the CFL during the simulation. At $t = 0\ s$, MPs are randomly distributed among RBCs with at-rest biconcave shape. As simulation progresses, at time $t = 1.7\ s$, RBCs start to deform and align their major axes along the shear direction (y-direction) under the shear stress of fluid flow. Besides, RBCs initially located near the wall gradually migrate to the center, leading to the formation of CFL. With simulation time further advancing, at $t = 3.4\ s$, more and more spherical MPs move from center of channel to CFL.

Interestingly, different shaped MPs demonstrate different performance during the above margination process. figure 8 presents the comparison of particle distribution along shear gradient direction (z-direction) between spherical and disc MPs. The bin width is 3 μm, which is chosen according to the thickness of CFL. Here the thicknesses of CFL has been calculated in the absence of MPs, which is about 2.8 μm for Ht = 30%. This is consistent with the previous simulation results (Lee et al. 2013; Müller et al. 2014). The particle concentration in the bin locating at bottom ($0 < z < 3\mu m$) represents MPs accumulating in the CFL. At the initial state ($t = 0\ s$), MPs concentrate around center region of channel with few locating in the CFL. We also confirm that MPs in CFL stay

within this near wall region and cannot demarginate to central stream of blood flow. At $t = 1.7\ s$, MPs start to marginate toward vessel wall and accumulate within the CFL. While the near-wall accumulation of spherical particle outperforms disc particle. As simulation time progresses, the marginations of both type of MPs continue but not significantly change. To further quantify the margination propensity, margination probability $\Phi(t)$ is defined to characterize the tendency, as:

$$\Phi(t) = \frac{n_f(t) - n_f(0)}{N}, \tag{22}$$

where n_f represents the number of MPs locating in CFL at time t, and N denotes the total number of MPs in the channel. The evolution of margination probabilities Φ for different shaped MPs are given in figure 9(a). In the end, the margination probabilities seem not high. It is because there are some particles initially located in the near-wall region as shown in figure 8 at time $t = 0\ s$. According to the definition of margination probability in Eq. (22), it characterizes the increment of MP accumulation in CFL. Therefore, there should be more MPs locating in the CFL comparing with the margination probability. Besides, we also find that the spherical particle demonstrate the highest margination probability, while disc particle is the lowest. The margination probabilities of other different shaped MPs have no obvious difference. This observation is not consistent with previous study (Vahidkhah and Bagchi 2015), in which the ellipsoidal particle demonstrates stronger margination than spherical particle. Such a difference could be induced by different shear rates. The shear rate in the previous work(Vahidkhah and Bagchi 2015) is 1000 s^{-1}, which is much higher than present study (200 s^{-1}).

To understand above observations, the mean square displacement (MSD) for MPs with different shapes is investigated. As we know, in the blood flow, the deformation of RBCs under shear stress can result in velocity fluctuation of the flow field around RBCs. This may be the major reason of particle migration in blood flow (Zhao et al. 2012). The cross-flow motion of MPs is diffusive, and we provide the evolution of MSD in figure 9(b). We find that MSDs for all particles are almost the same, and the diffusivity defined as $D =< \Delta z^2 > /2t$ ranges from about 4 to $5 \times 10^{-8} cm^{-2} s^{-1}$. This is consistent with previous studies (Vahidkhah and Bagchi 2015; Zhao and Shaqfeh 2011), and the

diffusivity of MPs is about 2 orders of magnitude higher than the Brownian diffusivity. It indicates that the existence of RBCs can enhance the diffusion of particles. However, from our simulation results, this RBC-enhanced diffusion is shape independent for MPs. Thus, the diffusion can not solely explain the shape-depended margination behavior of MPs.

The motion of MPs in blood flow is affected by two major forces: (i) viscous force due to shear flow; and (ii) collision force exerted by RBCs. It should be emphasized that the collision force exerted by RBCs on MPs is also fulfilled by the perturbation of flow field due to deformation of RBC. To determine which one dominates, these two factors are isolated to investigate through additional simulations. We remove RBCs from the channel, and only consider the movement of MPs in the shear flow under same conditions (identical shear rate, channel size, initial distribution of MPs, *etc.*). The migration of disc particle is given as an example in figure 10. The snapshots in figure 10(a) shows that initial randomly distributed disc MPs can migrate to the channel center as simulation advances. In particular, the MPs initially located in the near-wall region move toward the center region during the simulation. It is further confirmed by the distribution shown in figure 10(b). The particle concentration in the center region becomes larger, while in the near-wall regions, there is no MPs any more as simulation progresses. When only considering the viscous force coming from the fluid flow, MPs demonstrate the opposite tendency comparing with the margination behavior. Here, we name this type of motion as demargination. It is consistent with the result of a single particle dynamics in viscous flow (Leal 1980). Axisymmetric nonspherical particle generally migrates to the central stream in Couette flow through theoretical analysis. Furthermore, the shape dependence on the demargination behavior is investigated. The MSDs of different shaped MPs are calculated and presented in figure 11(a). We find that the diffusion of rod particle is the largest, and the spherical particle is the smallest. The diffusion of these particles is associated with the rotation, and nonspherical particles outperform spherical one through their rotation behavior under shear flow (Leal 1980). However, we also find that the diffusivity is one order of magnitude lower than that with RBCs (c.f. figure 9(b)). While it is still larger than the Brownian diffusivity. In other words, the shear induced migration of MPs hampers their margination behavior.

Then, we further explore the pair collision effect between a single RBC and a single MP. Note that the three-body and higher order collision schemes are not considered here. Because they can be negligible if the hematocrit of blood flow is not high ($< 45\%$) (Kumar and Graham 2012; Rivera et al. 2016; Qi and Shaqfeh 2017). The schematic of pair collision model is shown in figure 11(b). To eliminate the boundary effects, the channel size is enlarged with height 86 μm, width 27 μm and length 86 μm. The RBC and MP are placed in the center region of the channel. The distance between the initial positions of RBC and MP is set as $\sigma = 2$ μm. There are different collision modes depending on the direction of initial configuration of MP. For simplicity, only one collision mode is examined here. The major axes of RBC and MP (edge for cubic) are placed along the flow direction, and the symmetry rotation axis of RBC, disc, oblate MPs are along z-direction. We track the trajectories of centers of RBC and MP during the collision. The displacement of centers of RBC and MP along z-direction refers to the collision displacement (c.f. figure 11(c)). It should be noted that the velocity along flow direction of RBC is larger than that of MP, because center of RBC is higher than MP in z-direction ($u = \dot{\gamma} z$). Hence, the RBC would approach and collide with MP. After that, both of them laterally migrate, but towards the opposite directions. The MP demonstrates a larger lateral displacement than RBC, due to its small size. After the collision, MP tends to move towards its initial position, but reaches an equilibrium position rather than initial one. And the equilibrium position depends on the shape of MP. The distance between the equilibrium position and the initial position of MP is defined as collision displacement L_c. We summarize it for different shaped MPs in the figure 11(d). Besides, the margination probability without adhesion effect and the demargination probability without RBCs are also presented. As demargination is opposite to margination, its probability is always negative. To compare them in an easier way, we use $L_c/4$ to show collision displacement in the figure 11(d). From the comparison, we take some special cases to illustrate the interplay of viscous and collision forces on the motion of MPs in blood flow. As for the spherical particle, we find that the collision force is high, while the demargination is low, leading to the high margination probability of spherical MP. In terms of the rod particle, although the collision displacement is the largest, the demargination is also strong.

Hence, the margination probability of rod particle is relatively low, comparing with spherical one. This comparison also confirms that the margination behavior of MPs in blood flow is affected by the interplay of collision with RBCs and viscous effect. Thus, disc MP demonstrates the lowest margination, due to the small collision displacement and strong demargination.

Margination of MPs with adhesion

From figure 9(a), we can see that the margination probability increases and oscillates with time. It indicates that many MPs move between the central stream of blood flow and the CFL. Once MP reaches CFL, it has a chance to interact with the vessel wall, *i.e.* reaching adhesion layer. Therefore, the adhesion may affect the probability of MP to move away or towards vessel wall. The effect of adhesion is of significant especially for cases with thin CFL of blood flow and large size of MP. In present work, the thickness of CFL is about 2.8 μm, and the adhesion layer is about 0.8 μm. The size of MPs is comparable to, even larger than the thickness of CFL, shown in Table. 1. Thus, the adhesion effect on MP margination should be further studied in detail.

Figure 12(a) presents the margination behavior of spherical MP under influence of near-wall adhesion. We find that as simulation advances, more and more MPs accumulate in the CFL. Compared to the margination of spherical MP without adhesion in figure 9, there are more MPs in the CFL under the influence of adhesion. More importantly, the MPs in the CFL adhere on the substrate (or vessel wall). Note that the positions of MPs in the CFL vary along the vertical direction to the substrate in the case without adhesion. Furthermore, we plot the distributions of MPs along z-direction in the figure 12(b). The depletion of MPs in the center region and their accumulation in the CFL become more significant, compared to the case without adhesion (c.f. figure 8(a)). It signals that the near-wall adhesion plays a critical role in the MP margination within blood flow.

To quantify the influence of adhesion on margination behavior, the margination probability is adopted. While, to differentiate the margination probabilities with and without adhesion effect, we replace Φ with Π to represent the margination probability with adhesion effect. Figure 13(a) shows the evolution of margination probabilities for different shaped MPs. We find that spherical

and cubic particles demonstrate the highest margination probability, while the disc particle is the lowest. The tendency is comparable to the margination results without adhesion. Under the influence of adhesion effect, the difference of margination probabilities among MPs becomes apparent. It is obvious that oblate (AR=2) particle follows the cubic particle, and prolate (AR=2) particle outperforms prolate (AR=3) particle. To directly compare margination probabilities with and without adhesion, the averaged margination probabilities for both cases are presented in the figure 13(b). The time averaged value is calculated by averaging the margination probability in the last 0.1 s interval of the simulation. We find that adhesion can either promote (sphere, cubic, oblate (AR=2), prolate (AR=3) and prolate (AR=2)) or hamper (disc, rod and oblate (AR=3)) the margination behavior of MPs. The promotion of margination due to adhesion is straightforward that when MPs move nearby CFL, the adhesion force may capture these MPs. While the impediment to margination by adhesion is deserved to be further investigated.

First, the adhesion behavior of a single MP is studied, which is critical for understanding the adhesion effect on margination. Because the volume fraction of MPs is small, the MP-MP interaction is not important and negligible. We use a relatively small channel to conduct the adhesion study of a single MP. While only the dimension of channel changes to height 12 μm, width 9 μm and length 18 μm, other conditions such as shear rate, boundary condition *etc.* are kept the same. The MPs with different shapes are placed near the substrate with the major axes along shear direction. The minimum distance between MP and substrate is set as 1 μm. In the simulation, the strength of the individual biological bond is fixed, therefore the adhesion strength is reflected by the number of the biological bonds. Here we choose some typical cases to demonstrate the adhesion effect on margination behavior of MPs.

Figure 14(a) shows the evolution of margination probability of cubic particle with and without adhesion. At the initial stage ($t < 0.5$ s), the margination probabilities of both cases are similar. Afterwards, the adhesion effect starts to promote the margination behavior as simulation time progresses. Figure 14(b) shows the corresponding adhesion result on a single cubic particle near the substrate. We find that the cubic particle interact with the substrate through the whole simulation,

as the number of biological bonds is larger than 0. It indicates that when a cubic particle moves close to CFL, the particle may be captured by the substrate due to the ligand-receptor binding. Afterwards, the particle will not be able to move back to central stream of blood flow.

Furthermore, we compare the margination results for MPs with same shape but different aspect ratios, oblate particles with AR=2 and AR=3. Although they have the same shape, but the adhesion effect is opposite. The adhesion can promote margination of oblate particle with AR=2, while it hampers the margination of oblate with AR=3. Figure 15 shows the comparison of margination probability and adhesion strength between these two MPs. When AR=2, the adhesion starts to influence the margination at $t > 0.5\ s$. Although the promotion of margination is small, it keeps increasing through the simulation. The corresponding biological bonds is larger than zero. It signifies interaction between particle and substrate exists all the time. Increasing the aspect ratio to 3, at the initial time interval $0.5\ s < t < 1.75\ s$, the adhesion can enhance the margination. However, afterwards $t > 1.75\ s$, adhesion starts to hamper the margination behavior, resulting in the low margination of oblate particle with AR=3. We find that the evolution of number of biological bonds for oblate particle with AR=3 is not like that of oblate particle with AR=2. Figure 15(d) indicates that the number of bonds for oblate particle with AR=3 changes nearly periodical between 0 and about 60. Zero means no interaction between oblate particle and substrate. And under this circumstance, the particle's motion is not affected by the substrate. We also find that the duration of 0 is longer than that of 60. The time of the particle staying away from the substrate is longer than that interacting with substrate. This may be responsible to the impediment of adhesion on margination for oblate particle with AR=3. Further studies need to be performed for understanding this interesting phenomenon.

Mechanism of adhesion effect on margination behavior

When MP moves close to substrate, it will tumble under the shear flow due to asymmetry of flows in the upper and lower sides of the particle (Leal 1980). Note that spherical particle will roll rather than tumble under the same circumstance. Figure 16 is a simple schematic to illustrate the tumbling behavior of particle near the substrate. We focus on the trajectories of particle center and

maximum distance between particle and substrate, which correspond to O_1 to O_5 and M_1 to M_5, respectively. The center trajectory gives the position of MP, and we can know whether it is in the CFL or not. Through comparing the maximum distance with the thickness of CFL, if the maximum distance is larger than CFL thickness, the MP will interact with RBCs. Otherwise, the motion of MP is governed by shear flow and adhesion.

Figure 17(a) shows the distribution of major axes of MPs. The dashed line denotes the thickness of CFL. It divides MPs into two classes, major axes larger (rod, oblate (AR=3), prolate (AR=2) and prolate (AR=3)) and smaller (sphere, cubic, disc and oblate (AR=2)) than CFL thickness. The evolutions of maximum distance and center position of cubic, oblate with two aspect ratios are presented in figure 17(b). We can see that the maximum distance of cubic particle is within the CFL. While oblate particles have the larger maximum distance than CFL thickness, although the difference between maximum distance and CFL thickness is not obvious. However, this result can not solely explain the above margination results, which might be induced by the shear flow rather than the adhesion. Thus we conduct the same simulations for a single MP near substrate but without adhesion. We extract the trajectory results to make a comparison with particle motion under adhesion. Figure 18 displays the comparison of trajectory and maximum distance of a single particle motion near substrate with and without adhesion. We find that the cubic particle will migrate away from the substrate without adhesion, which confirms that adhesion can capture the cubic particle and keep it within CFL. And there is not interaction between the cubic particle and RBCs once it enters CFL. Thus, adhesion promotes the margination behavior of cubic particle. As for disc, rod and oblate (AR=3), the adhesion prevents their migration away from substrate. However, their maximum distances show that they will interact with RBCs. While the oblate (AR=2) has a decrease of maximum distance, which makes the maximum distance lower than the thickness of CFL. Even though the maximum distance of prolate (AR=3) is always larger than CFL thickness, the maximum distance continues to decrease with simulation time advancing.

In the figure 18, from the characteristics of tumbling trajectories of MPs, we find that the tumbling frequency changes under the influence of near-wall adhesion. The tumbling frequencies

of MPs are calculated for dynamics of a single particle with and without adhesion, as shown in figure 19. We find that the adhesion will reduce the tumbling frequency of MPs. For sphere, cubic, and oblate (AR=2) particles, the entire body locates within CFL. Therefore, the low tumbling motion promotes their adhesion. These MPs can firmly adhere on the substrate, leading to enhancement of their margination. For the other MPs, the maximum distance results show that, during the tumbling motion, they will interact with RBCs. This interaction may drag them from CFL to the center region of the channel. Furthermore, the evolution of number of bonds reveals that in one tumbling period, there is no bond formation in some time intervals, which means no interaction between substrate and MPs. And at other time intervals, due to reduced tumbling frequency, MPs have longer time to interact with RBCs. Then MPs have a larger chance to leave from CFL under the dragging of RBCs.

However, the prolate particles are exceptions. This may be induced by the irregular tumbling motion of prolate particles. From figure 18(f), we can find that, besides the tumbling motion, precession happens for prolate particles according to the evolution of maximum distance. We compare the snapshots of particle motion between rod and prolate (AR=3). Here, the rod is chosen as its shape is close to prolate (AR=3). Figure 20 provides the comparison of tumbling motions between rod and prolate (AR=3) under adhesion effect in one period. We find that rod particle regularly tumbles with major axis on the y-z plane through the simulation. When the prolate particle tumbles, the major axis can not keep on the y-z plane. There exists precession for the prolate particle, which is shown in Figure 20. The semi-transparent snapshots and black dashed lines denote position and major axis under the regular tumbling motion, respectively. The red dashed lines represent the actual position of major axis. This precession will further reduce the maximum distance of prolate particle, and some equilibrium states may exist. The prolate particle may align its major axis in the x-z plane. This will make the maximum distance equal to minor axis length. Besides, the decrease of maximum distance is more significant than that without adhesion, which means adhesion accelerates the transition from regular tumbling motion to precession motion. Thus, adhesion can enhance the margination of prolate particles.

CONCLUSION

We use the three-dimensional numerical simulations to study the shape effect of MPs on their margination behavior. Margination probability is adopted to quantify the margination process of MPs. The shape dependence of MP margination without adhesion is firstly investigated. We find that the spherical particle has the largest margination probability among the different shaped MPs. To understand this phenomenon, migration behaviors of MPs without RBCs in the shear flow are studied. We find that demargination happens for all the different shaped MPs, which is induced by the asymmetry of the shear flow around MPs near the vessel wall. Additionally, the collision numerical experiments are conducted between a single RBC and a single MP. We find that the rod particle has the largest collision displacement. Combining the demargination performance and collision displacement, the largest margination probability of spherical particle is attributed to its low demargination and large collision displacement.

Furthermore, the near-wall adhesion effect is considered. We find that adhesion can either promote or hamper margination behaviors of MPs depending on their shapes. The underlying mechanism is explained as follows. When the major axes of MPs is smaller than or comparable to the CFL thickness, the adhesion can promote the margination. While for MPs with a large major axes, the adhesion can reduce the tumbling frequencies of MPs near the substrate, and then give them enough time to interact with RBCs. The long time interaction with RBCs may drag them to central stream of blood flow, hampering their margination. However, the prolate particles demonstrate distinct behaviors. Apart from tumbling, the transition to precession for prolate particles near the substrate results in the enhancement of their margination. We should emphasize that the present study is restricted to moderate shear flow rate and micro-size particle. This study might offer theoretical guidance to design MP-based drug carriers in blood flow with high efficacy.

REFERENCES

Belytschko, T., Liu, W. K., Moran, B., and Elkhodary, K. (2013). Nonlinear finite elements for continua and structures. John wiley & sons.

638 Bhagat, A. A. S., Bow, H., Hou, H. W., Tan, S. J., Han, J., and Lim, C. T. (2010). "Microfluidics
639 for cell separation." Med. Biol. Eng. Comput., 48(10), 999–1014.
640 Blanco, E., Shen, H., and Ferrari, M. (2015). "Principles of nanoparticle design for overcoming
641 biological barriers to drug delivery." Nature biotechnology, 33(9), 941.
642 Chen, S. and Doolen, G. D. (1998). "Lattice boltzmann method for fluid flows." Annu. Rev. Fluid
643 Mech., 30(1), 329–364.
644 Decuzzi, P. and Ferrari, M. (2006). "The adhesive strength of non-spherical particles mediated by
645 specific interactions." Biomaterials, 27(30), 5307–5314.
646 Decuzzi, P., Godin, B., Tanaka, T., Lee, S.-Y., Chiappini, C., Liu, X., and Ferrari, M. (2010).
647 "Size and shape effects in the biodistribution of intravascularly injected particles." Journal of
648 Controlled Release, 141(3), 320–327.
649 Decuzzi, P., Lee, S., Bhushan, B., and Ferrari, M. (2005). "A theoretical model for the margination
650 of particles within blood vessels." Annals of biomedical engineering, 33(2), 179–190.
651 Decuzzi, P., Pasqualini, R., Arap, W., and Ferrari, M. (2009). "Intravascular delivery of particulate
652 systems: does geometry really matter?." Pharmaceutical research, 26(1), 235.
653 Donea, J., Giuliani, S., and Halleux, J.-P. (1982). "An arbitrary lagrangian-eulerian finite ele-
654 ment method for transient dynamic fluid-structure interactions." Computer methods in applied
655 mechanics and engineering, 33(1-3), 689–723.
656 Fåhræus, R. and Lindqvist, T. (1931). "The viscosity of the blood in narrow capillary tubes." Am.
657 J. Physiol., 96(3), 562–568.
658 Farutin, A. and Misbah, C. (2013). "Analytical and numerical study of three main migration laws
659 for vesicles under flow." Physical review letters, 110(10), 108104.
660 Fedosov, D. A. (2010). Multiscale modeling of blood flow and soft matter. Brown University.
661 Fedosov, D. A., Caswell, B., and Karniadakis, G. E. (2010a). "A multiscale red blood cell model
662 with accurate mechanics, rheology, and dynamics." Biophys. J., 98(10), 2215–2225.
663 Fedosov, D. A., Caswell, B., and Karniadakis, G. E. (2011a). "Wall shear stress-based model for
664 adhesive dynamics of red blood cells in malaria." Biophys. J., 100(9), 2084–2093.

Fedosov, D. A., Caswell, B., Popel, A. S., and Karniadakis, G. E. (2010b). "Blood flow and cell-free layer in microvessels." Microcirculation, 17(8), 615–628.

Fedosov, D. A., Fornleitner, J., and Gompper, G. (2012). "Margination of white blood cells in microcapillary flow." Physical review letters, 108(2), 028104.

Fedosov, D. A., Pan, W., Caswell, B., Gompper, G., and Karniadakis, G. E. (2011b). "Predicting human blood viscosity in silico." Proc. Natl. Acad. Sci. U.S.A., 108(29), 11772–11777.

Feng, Z.-G. and Michaelides, E. E. (2004). "The immersed boundary-lattice boltzmann method for solving fluid–particles interaction problems." J. Comput. Phys., 195(2), 602–628.

Ferziger, J. H. and Peric, M. (2012). Computational methods for fluid dynamics. Springer Science & Business Media.

Firrell, J. C. and Lipowsky, H. H. (1989). "Leukocyte margination and deformation in mesenteric venules of rat." American Journal of Physiology-Heart and Circulatory Physiology, 256(6), H1667–H1674.

Fischer, T. M. (2004). "Shape memory of human red blood cells." Biophys. J., 86(5), 3304–3313.

Fischer, T. M. (2007). "Tank-tread frequency of the red cell membrane: dependence on the viscosity of the suspending medium." Biophys. J., 93(7), 2553–2561.

Gentile, F., Chiappini, C., Fine, D., Bhavane, R., Peluccio, M., Cheng, M. M.-C., Liu, X., Ferrari, M., and Decuzzi, P. (2008). "The effect of shape on the margination dynamics of non-neutrally buoyant particles in two-dimensional shear flows." Journal of biomechanics, 41(10), 2312–2318.

Goldsmith, H. L. and Spain, S. (1984). "Margination of leukocytes in blood flow through small tubes." Microvascular research, 27(2), 204–222.

Gossett, D. R., Weaver, W. M., Mach, A. J., Hur, S. C., Tse, H. T. K., Lee, W., Amini, H., and Di Carlo, D. (2010). "Label-free cell separation and sorting in microfluidic systems." Anal. Bioanal.Chem., 397(8), 3249–3267.

Guo, Z., Zheng, C., and Shi, B. (2002). "Discrete lattice effects on the forcing term in the lattice boltzmann method." Phys. Rev. E, 65(4), 046308.

Hammer, D. A. and Lauffenburger, D. A. (1987). "A dynamical model for receptor-mediated cell

692 adhesion to surfaces." Biophys. J., 52(3), 475–487.

693 Hou, H. W., Bhagat, A. A. S., Chong, A. G. L., Mao, P., Tan, K. S. W., Han, J., and Lim,
694 C. T. (2010). "Deformability based cell margination—a simple microfluidic design for malaria-
695 infected erythrocyte separation." Lab. Chip, 10(19), 2605–2613.

696 Hughes, T. J., Liu, W. K., and Zimmermann, T. K. (1981). "Lagrangian-eulerian finite element
697 formulation for incompressible viscous flows." Computer methods in applied mechanics and
698 engineering, 29(3), 329–349.

699 Krüger, T., Varnik, F., and Raabe, D. (2011). "Efficient and accurate simulations of deformable
700 particles immersed in a fluid using a combined immersed boundary lattice boltzmann finite
701 element method." Comput. Math. Appl., 61(12), 3485–3505.

702 Kumar, A. and Graham, M. D. (2012). "Margination and segregation in confined flows of blood
703 and other multicomponent suspensions." Soft Matter, 8(41), 10536–10548.

704 Leal, L. (1980). "Particle motions in a viscous fluid." Annual Review of Fluid Mechanics, 12(1),
705 435–476.

706 Lee, S.-Y., Ferrari, M., and Decuzzi, P. (2009). "Shaping nano-/micro-particles for enhanced
707 vascular interaction in laminar flows." Nanotechnology, 20(49), 495101.

708 Lee, T.-R., Choi, M., Kopacz, A. M., Yun, S.-H., Liu, W. K., and Decuzzi, P. (2013). "On the
709 near-wall accumulation of injectable particles in the microcirculation: smaller is not better." Sci.
710 Rep., 3, 2079.

711 Ley, K. and Tedder, T. F. (1995). "Leukocyte interactions with vascular endothelium. new insights
712 into selectin-mediated attachment and rolling.." J. Immunol., 155(2), 525–528.

713 Li, P., Mao, Z., Peng, Z., Zhou, L., Chen, Y., Huang, P.-H., Truica, C. I., Drabick, J. J., El-Deiry,
714 W. S., Dao, M., et al. (2015). "Acoustic separation of circulating tumor cells." Proceedings of
715 the National Academy of Sciences, 112(16), 4970–4975.

716 Li, Y., Lian, Y., Zhang, L. T., Aldousari, S. M., Hedia, H. S., Asiri, S. A., and Liu, W. K. (2016).
717 "Cell and nanoparticle transport in tumour microvasculature: the role of size, shape and surface
718 functionality of nanoparticles." Interface focus, 6(1), 20150086.

719 Li, Y., Stroberg, W., Lee, T.-R., Kim, H. S., Man, H., Ho, D., Decuzzi, P., and Liu, W. K.
720 (2014). "Multiscale modeling and uncertainty quantification in nanoparticle-mediated drug/gene
721 delivery." Computational Mechanics, 53(3), 511–537.
722 Liu, Y. and Liu, W. K. (2006). "Rheology of red blood cell aggregation by computer simulation."
723 Journal of Computational Physics, 220(1), 139–154.
724 Mackay, F., Ollila, S. T., and Denniston, C. (2013). "Hydrodynamic forces implemented into
725 lammps through a lattice-boltzmann fluid." Comput. Phys. Commun., 184(8), 2021–2031.
726 MacMECCAN, R. M., Clausen, J., Neitzel, G., and Aidun, C. (2009). "Simulating deformable
727 particle suspensions using a coupled lattice-boltzmann and finite-element method." J. Fluid
728 Mech., 618, 13.
729 Mittal, R. and Iaccarino, G. (2005). "Immersed boundary methods." Annu. Rev. Fluid Mech., 37,
730 239–261.
731 Müller, K., Fedosov, D. A., and Gompper, G. (2014). "Margination of micro-and nano-particles in
732 blood flow and its effect on drug delivery." Sci. Rep., 4, 4871.
733 Müller, K., Fedosov, D. A., and Gompper, G. (2016). "Understanding particle margination in blood
734 flow–a step toward optimized drug delivery systems." Med. Eng. Phys., 38(1), 2–10.
735 Nadler, S. B., Hidalgo, J. U., and Bloch, T. (1962). "Prediction of blood volume in normal human
736 adults." Surgery, 51(2), 224–232.
737 Ollila, S. T., Denniston, C., Karttunen, M., and Ala-Nissila, T. (2011). "Fluctuating lattice-
738 boltzmann model for complex fluids." J. Chem. Phys., 134(6), 064902.
739 Papaioannou, T. G. and Stefanadis, C. (2005). "Vascular wall shear stress: basic principles and
740 methods." Hellenic J Cardiol, 46(1), 9–15.
741 Persson, P.-O. (2005). "Mesh generation for implicit geometries." Ph.D. thesis, Massachusetts
742 Institute of Technology, Massachusetts Institute of Technology.
743 Persson, P.-O. and Strang, G. (2004). "A simple mesh generator in matlab." SIAM review, 46(2),
744 329–345.
745 Peskin, C. S. (1972). "Flow patterns around heart valves: a numerical method." J. Comput. Phys.,

10(2), 252–271.

Peskin, C. S. (2002). "The immersed boundary method." Acta Numer., 11, 479–517.

Plimpton, S. (1995). "Fast parallel algorithms for short-range molecular dynamics." J. Comput. Phys., 117(1), 1–19.

Qi, Q. M. and Shaqfeh, E. S. (2017). "Theory to predict particle migration and margination in the pressure-driven channel flow of blood." Physical Review Fluids, 2(9), 093102.

Ramakrishnan, N., Wang, Y., Eckmann, D. M., Ayyaswamy, P. S., and Radhakrishnan, R. (2017). "Motion of a nano-spheroid in a cylindrical vessel flow: Brownian and hydrodynamic interactions." J. Fluid Mech., 821, 117–152.

Rivera, R. G. H., Zhang, X., and Graham, M. D. (2016). "Mechanistic theory of margination and flow-induced segregation in confined multicomponent suspensions: simple shear and poiseuille flows." Physical Review Fluids, 1(6), 060501.

Suresh, S., Spatz, J., Mills, J., Micoulet, A., Dao, M., Lim, C., Beil, M., and Seufferlein, T. (2015). "Reprint of: connections between single-cell biomechanics and human disease states: gastrointestinal cancer and malaria." Acta Biomater., 23, S3–S15.

Tan, J., Thomas, A., and Liu, Y. (2012). "Influence of red blood cells on nanoparticle targeted delivery in microcirculation." Soft Matter, 8(6), 1934–1946.

Thompson, A. J., Mastria, E. M., and Eniola-Adefeso, O. (2013). "The margination propensity of ellipsoidal micro/nanoparticles to the endothelium in human blood flow." Biomaterials, 34(23), 5863–5871.

Tokarev, A., Butylin, A., and Ataullakhanov, F. (2011). "Platelet adhesion from shear blood flow is controlled by near-wall rebounding collisions with erythrocytes." Biophysical journal, 100(4), 799–808.

Toy, R., Hayden, E., Shoup, C., Baskaran, H., and Karathanasis, E. (2011). "The effects of particle size, density and shape on margination of nanoparticles in microcirculation." Nanotechnology, 22(11), 115101.

Vahidkhah, K. and Bagchi, P. (2015). "Microparticle shape effects on margination, near-wall

dynamics and adhesion in a three-dimensional simulation of red blood cell suspension." Soft Matter, 11(11), 2097–2109.

Vahidkhah, K., Diamond, S. L., and Bagchi, P. (2014). "Platelet dynamics in three-dimensional simulation of whole blood." Biophysical journal, 106(11), 2529–2540.

Ye, H., Huang, H., Sui, Y., and Lu, X.-Y. (2016). "Dynamics of a nonspherical capsule in general flow." Computers & Fluids, 134, 31–40.

Ye, H., Shen, Z., and Li, Y. (2017a). "Cell stiffness governs its adhesion dynamics on substrate under shear flow." IEEE Trans. Nanotechnol.

Ye, H., Shen, Z., and Li, Y. (2017b). "Computational modeling of magnetic particle margination within blood flow through lammps." Comput. Mech., 1–20.

Ye, H., Shen, Z., Yu, L., Wei, M., and Li, Y. (2017c). "Anomalous vascular dynamics of nanoworms within blood flow." ACS Biomater. Sci. Eng.

Ye, H., Shen, Z., Yu, L., Wei, M., and Li, Y. (2018). "Manipulating nanoparticle transport within blood flow through external forces: an exemplar of mechanics in nanomedicine." Proc. R. Soc. A, 474(2211), 20170845.

Ye, H., Wei, H., Huang, H., and Lu, X.-y. (2017d). "Two tandem flexible loops in a viscous flow." Phys. Fluids, 29(2), 021902.

Zhao, H. and Shaqfeh, E. S. (2011). "Shear-induced platelet margination in a microchannel." Phys. Rev. E, 83(6), 061924.

Zhao, H., Shaqfeh, E. S., and Narsimhan, V. (2012). "Shear-induced particle migration and margination in a cellular suspension." Phys. Fluids, 24(1), 011902.

List of Tables

Shape	Volume (μm^3)	Area (μm^2)	Major axis (μm)	Vertexes	Elements
I. RBC	96	135	4.9	3286	6568
II. Sphere	4.18	12.52	2.0	828	1652
III. Rod	4.18	14.52	3.63	856	1708
IV. Cubic	4.18	12.65	1.61 *	672	1340
V. Disc	4.18	14.65	2.52	828	1652
VI. Oblate (AR=3)	4.18	15.7	2.88	956	1908
VII. Oblate (AR=2)	4.18	13.7	2.51	880	1756
VIII. Prolate (AR=3)	4.18	14.78	4.16	932	1860
IX. Prolate (AR=2)	4.18	13.48	3.17	860	1716
$*$ represents the length of the cubic particle					

TABLE 1. Properties of RBC and different shaped MPs.

Parameters	Simulation	Physical
RBC diameter (D_r)	32	$8 \times 10^{-6}\ m$
RBC shear modulus (μ_r)	0.01	$6.3 \times 10^{-6}\ N/m$
Energy scale ($k_{\mathrm{B}}T$)	1.1×10^{-4}	$4.14 \times 10^{-21}\ N \cdot m$
Viscosity of fluid (η)	0.167	$0.0012\ Pa \cdot s$
Area constant (k_a)	0.0075	$4.72 \times 10^{-6}\ N/m$
Local area constant (k_d)	0.367	$2.31 \times 10^{-4}\ N/m$
Volume constant (k_v)	0.096	$249\ N/m^2$
RBC bending constant (k_b)	0.013	$5 \times 10^{-19}\ N \cdot m$

TABLE 2. Coarse-grained potential parameters for red blood cells and their corresponding physical values.

Parameters	Simulation	Physical
MP shear modulus (μ_r)	1.0	$6.3 \times 10^{-4}\ N/m$
Area constant (k_a)	0.075	$4.72 \times 10^{-5}\ N/m$
Local area constant (k_d)	3.67	$2.31 \times 10^{-3}\ N/m$
Volume constant (k_v)	0.96	$2490\ N/m^2$
Bending constant (k_b)	0.13	$5 \times 10^{-18}\ N \cdot m$

TABLE 3. Coarse-grained potential parameters for MPs and their corresponding physical values.

Parameters	Simulation	Physical
Equilibrium length of bond (l_0)	1	250 nm
Bond strength (k_s)	5×10^{-5}	3.15×10^{-8} N/m
Reactive and rupture distance (d_{on} and d_{off})	4	$1\mu m$
On strength (σ_{on})	0.7305	1.9×10^{-7} N/m
Off strength (σ_{off})	0.7305	1.9×10^{-7} N/m
Unstressed on rate (k^0_{on})	3.75	1.3×10^{6} s^{-1}
Unstressed off rate (k^0_{off})	0.05	1.8×10^{4} s^{-1}
Ligand density (n_l)	4.11	66 $mol/\mu m^2$
Receptor density (n_r)	1.0	16 $mol/\mu m^2$

TABLE 4. Parameters used in adhesive model for ligand-receptor binding.

List of Figures

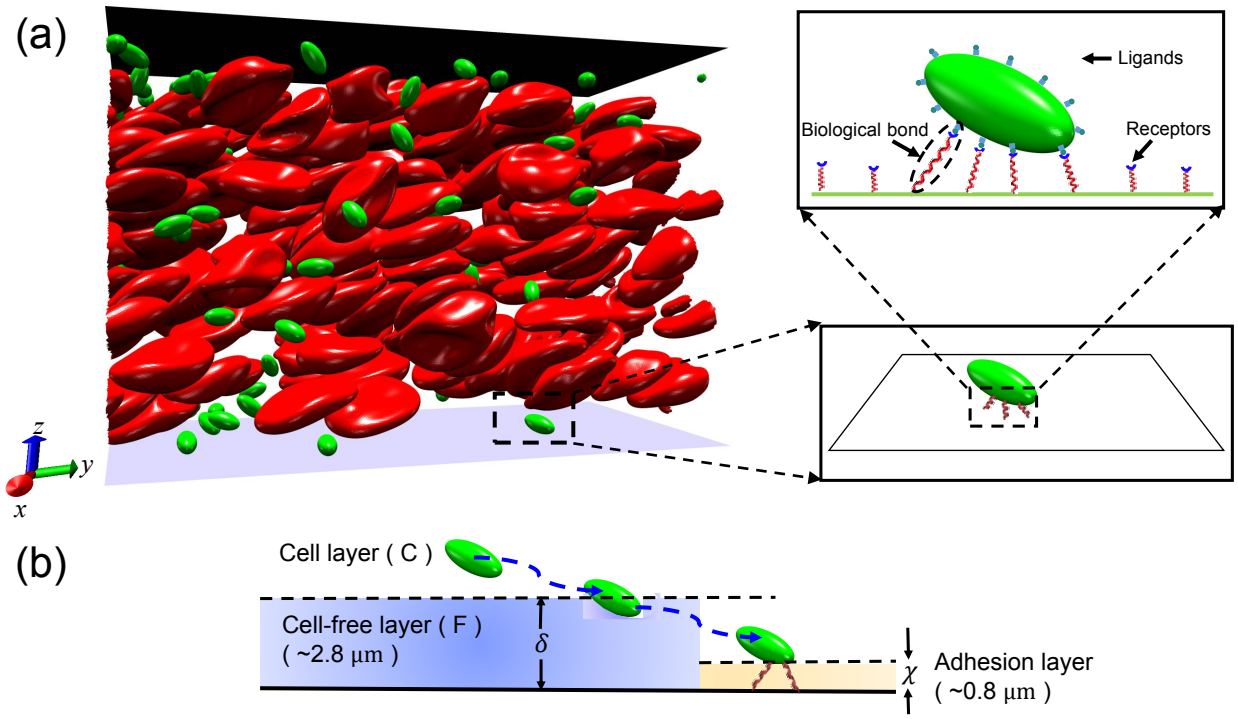

Fig. 1. Transport of MPs in blood flow. (*a*) Computational model for margination and adhesion of MPs in blood flow. Zoom-in figures give the detailed adhesion behavior of a MP under ligand-receptor binding. (*b*) Schematic of transport process of a MP from cell center (denoted as C) to cell-free layer (F), and then reaching adhesion layer.

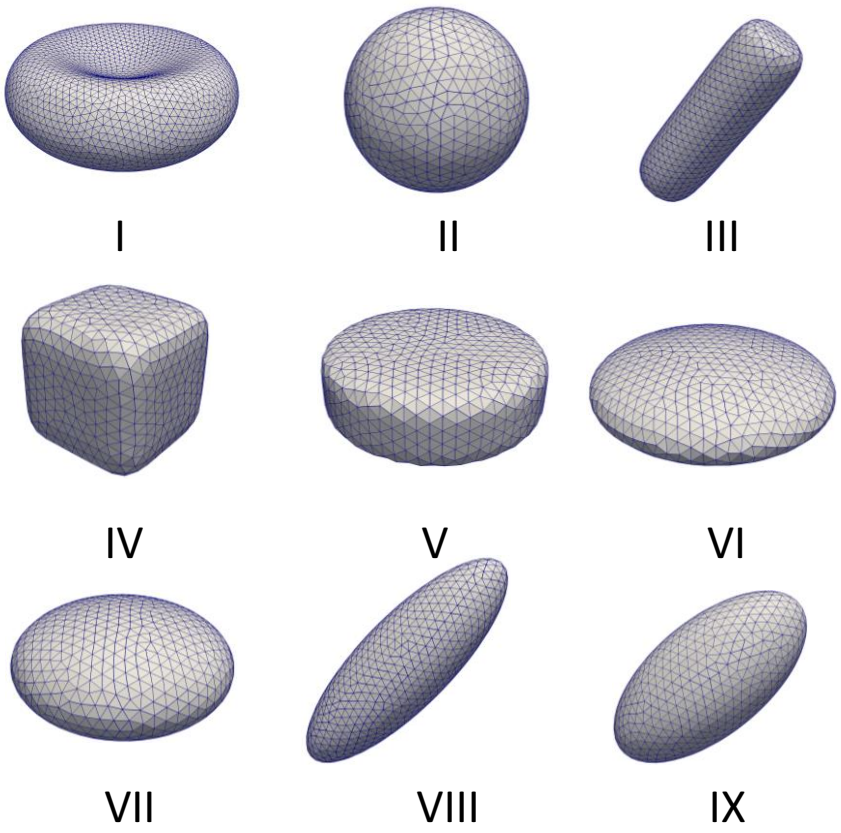

Shape
I. RBC
II. Sphere
III. Rod
IV. Cubic
V. Disc
VI. Oblate (AR=3)
VII. Oblate (AR=2)
VIII. Prolate (AR=3)
IX. Prolate (AR=2)

Fig. 2. Computational models for RBC and different shaped MPs: I. RBC, II. Sphere, III. Rod, IV. Cubic, V. Disc, VI. Oblate (AR=3), VII. Oblate (AR=2), VIII. Prolate (AR=3), IX. Prolate (AR=2).

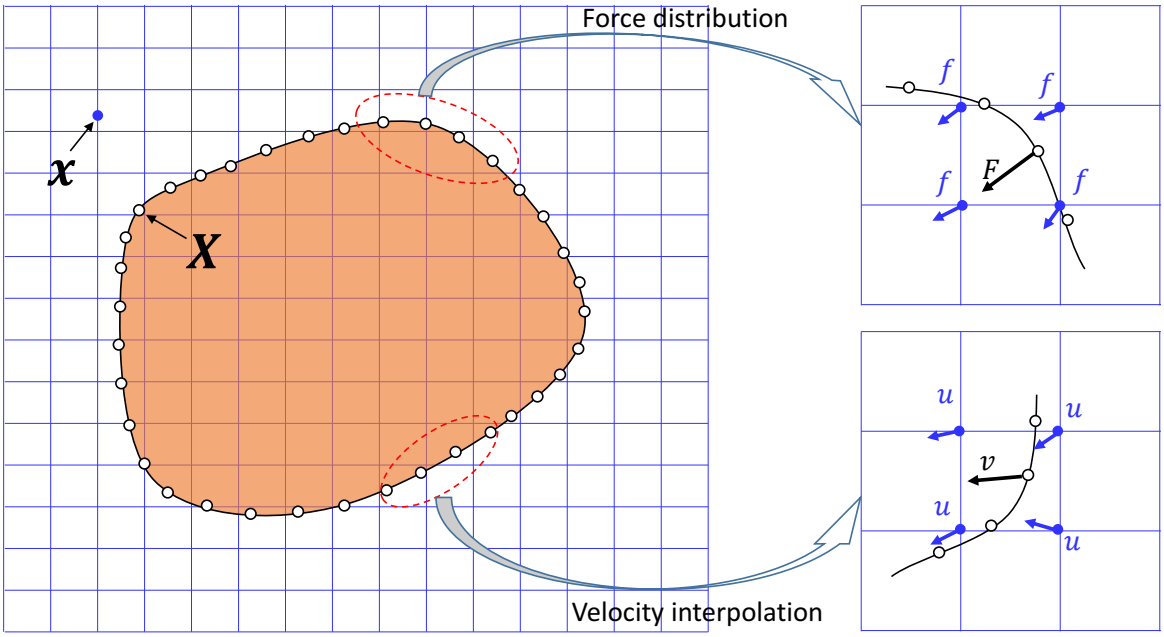

Fig. 3. Numerical scheme of the immersed boundary method (IBM). Solid squares represent the Eulerian fluid points (x), and solid circles denote vertices of Lagrangian membrane ($\mathbf{X}$).

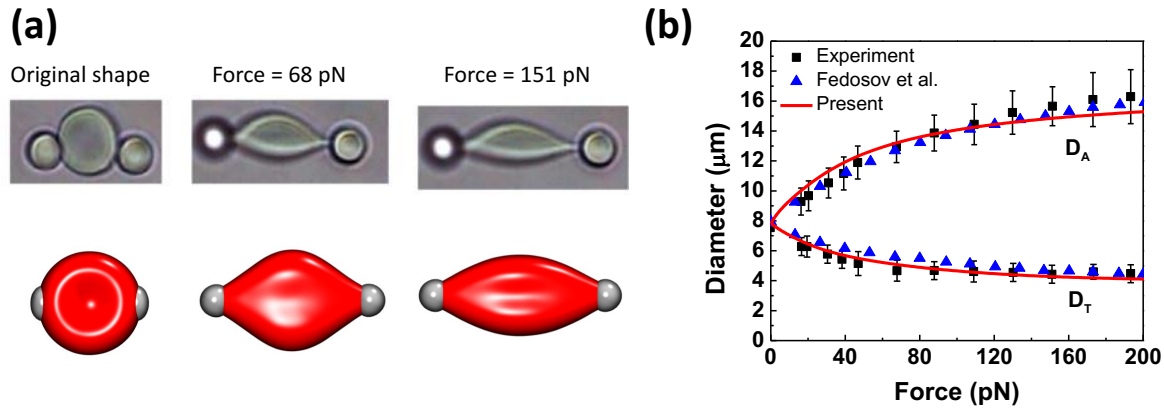

Fig. 4. Stretching test of a single RBC. (a) Configuration of stretched RBC with different applied forces. (b) Diameters of RBC along stretching direction and transverse direction, denoted by D_A and D_T, respectively.

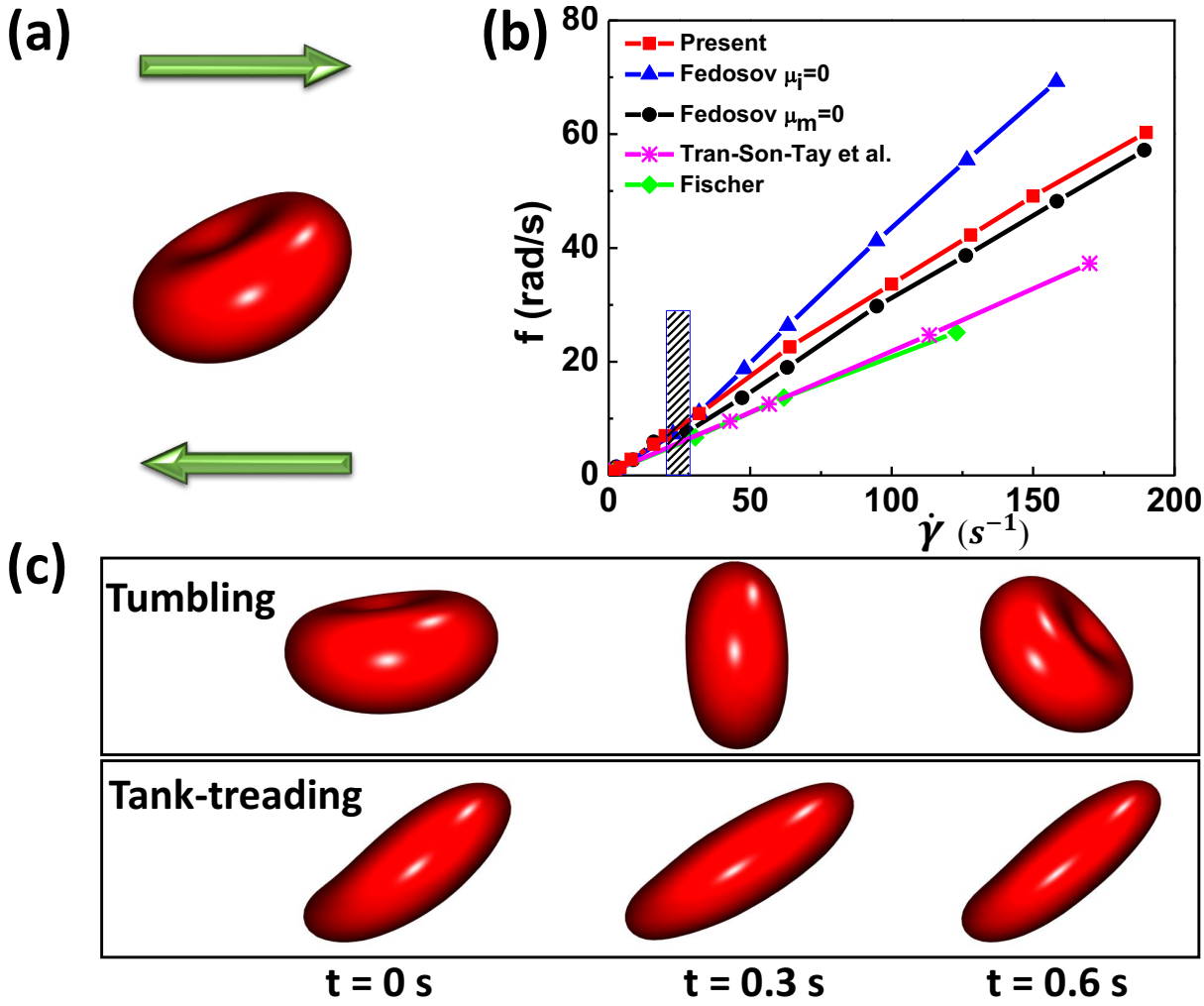

Fig. 5. Tank-treading and tumbling of a single RBC in shear flow. (a) Schematic of a single RBC in shear flow driven by moving of upper and bottom plates with the same velocity but opposite direction. (b) Tank-treading and tumbling frequency of RBC under different shear rates. (c) Snapshots of tumbling and tank-treading behaviors of RBC. In (b), μ_i and μ_m represent the inner flow viscosity and membrane viscosity, respectively.

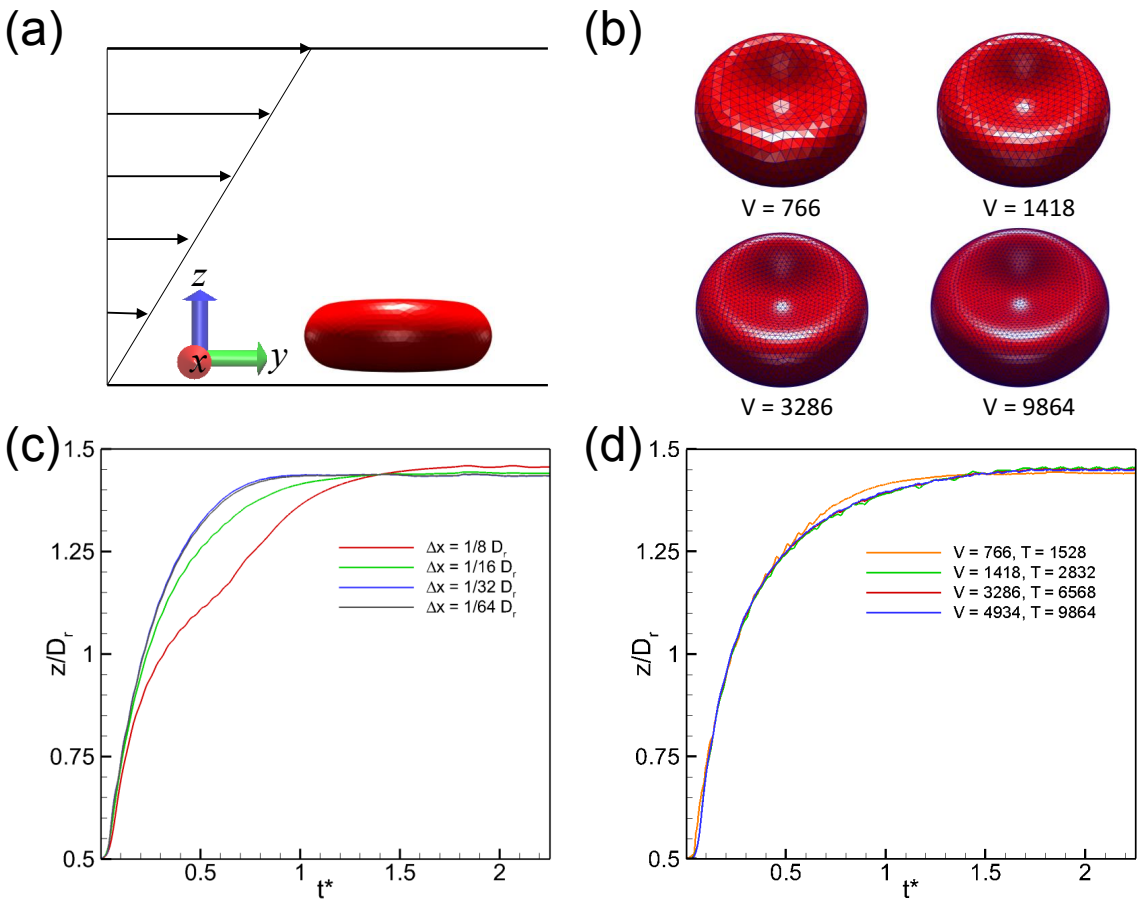

Fig. 6. Grid independence studies. (a) Schematic of a single RBC in simple shear flow. (B) Discretization of RBC membrane with different vertexes. (c) Grid independence of fluid mesh. (d) Grid independence of RBC discretization.

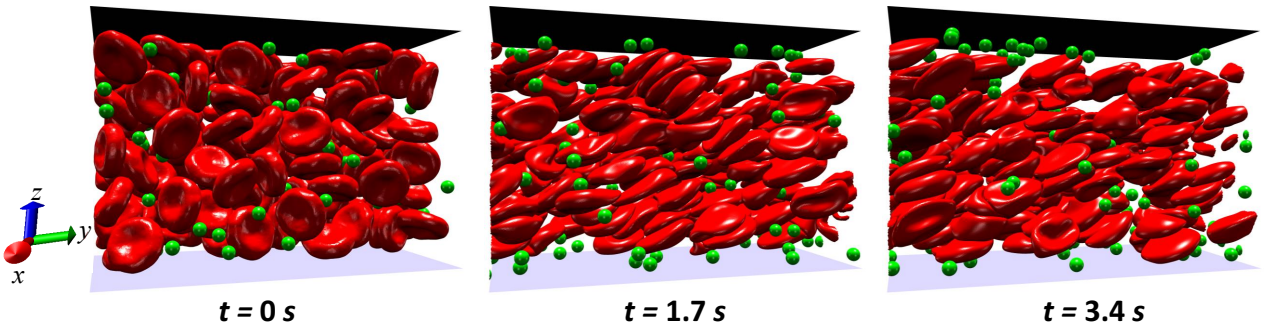

Fig. 7. Snapshots for the margination behavior of spherical MPs without adhesion.

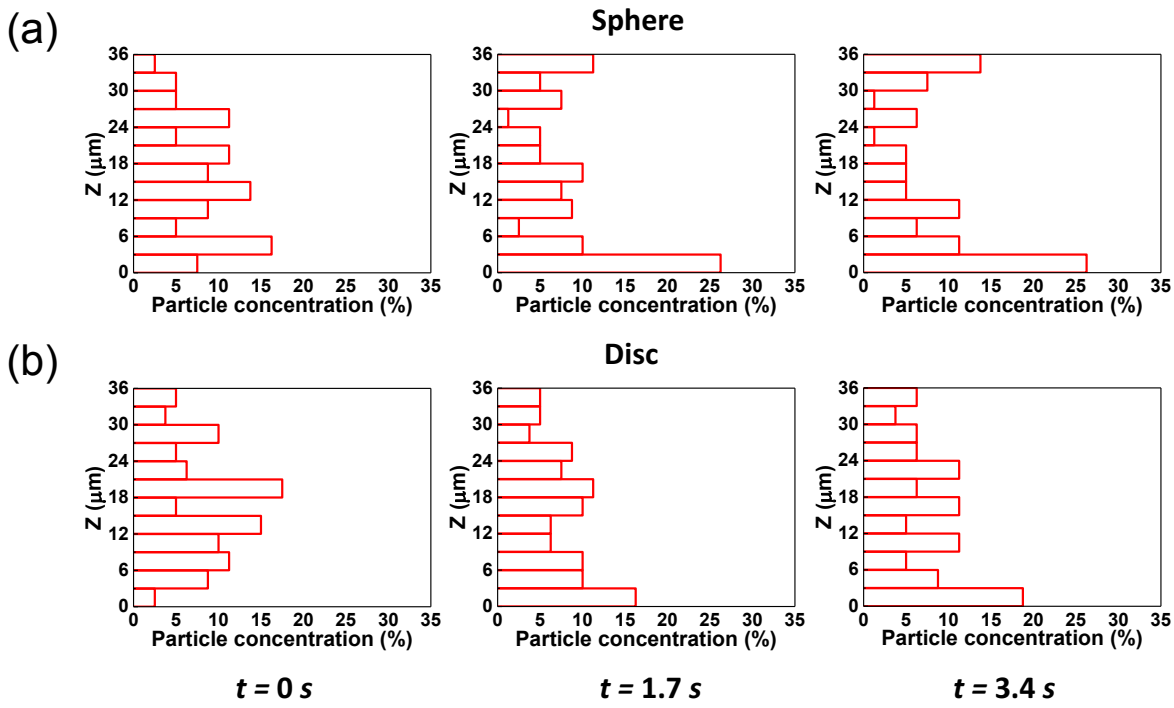

Fig. 8. Distribution of particle concentrations along the shear gradient direction (z-direction) for (a) spherical particle and (b) disc particle.

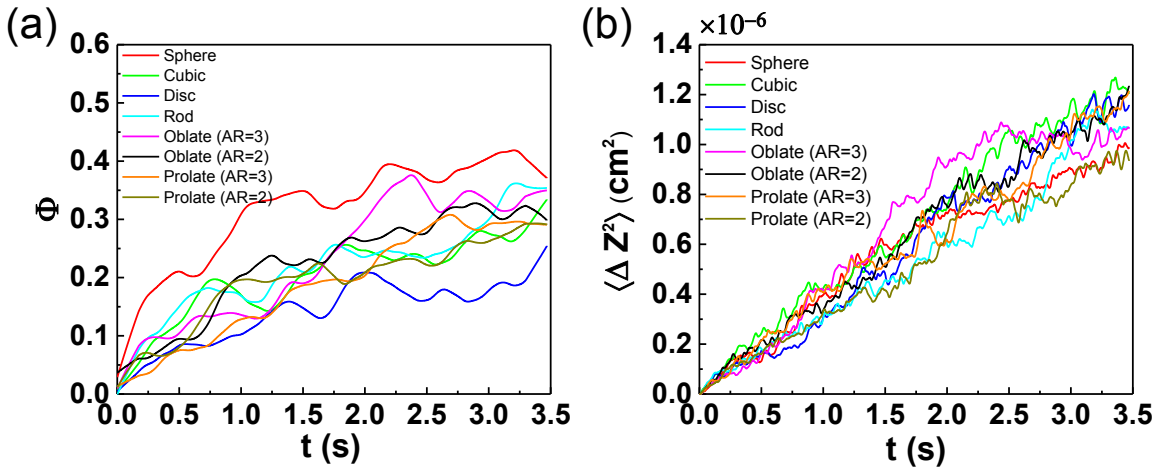

Fig. 9. (a) Evolution of margination probabilities for different shaped MPs. (b) Evolution of MSD of all shaped MPs.

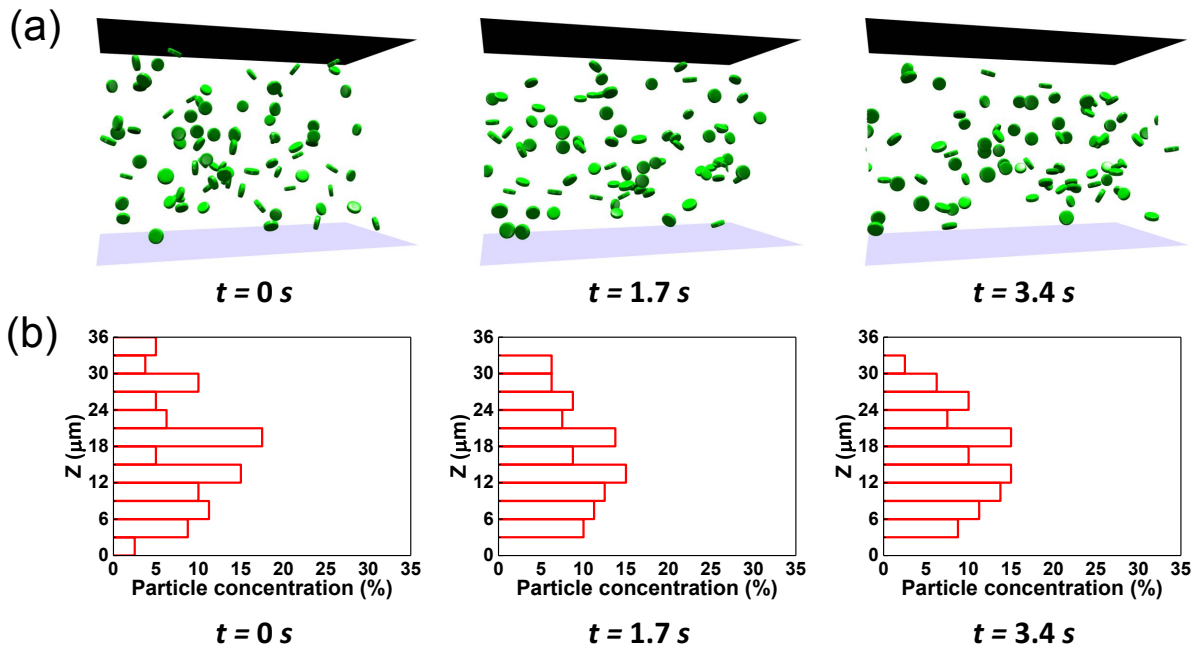

Fig. 10. Motion of disc MPs in the flow without RBCs. (a) Snapshots for the motion of disc shape particle. (b) Distribution of disc particle concentrations along the shear gradient direction (z-direction).

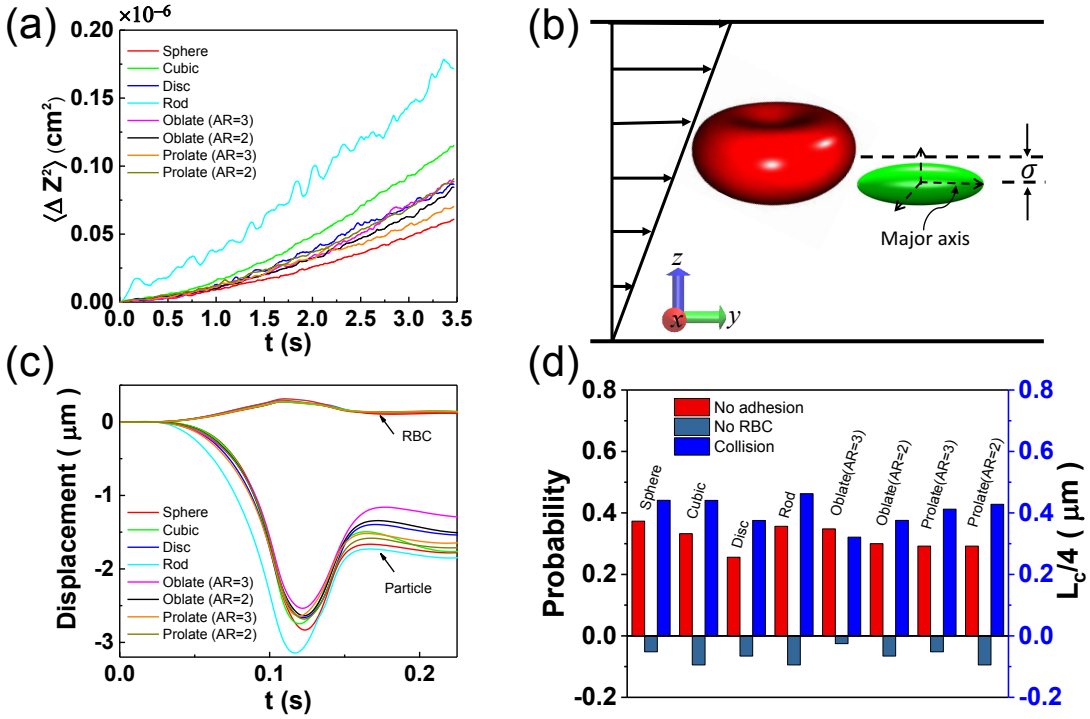

Fig. 11. (a) MSDs for MPs in the flow without RBCs. (b) Pair collision model between a single RBC and a MP with initial center distance σ. The major axis of RBC or MP is initially placed along flow direction. (c) Collision displacements in the shear gradient direction for RBCs and MPs after collision. (d) Comparison among the margination probability, demargination probability and collision displacement.

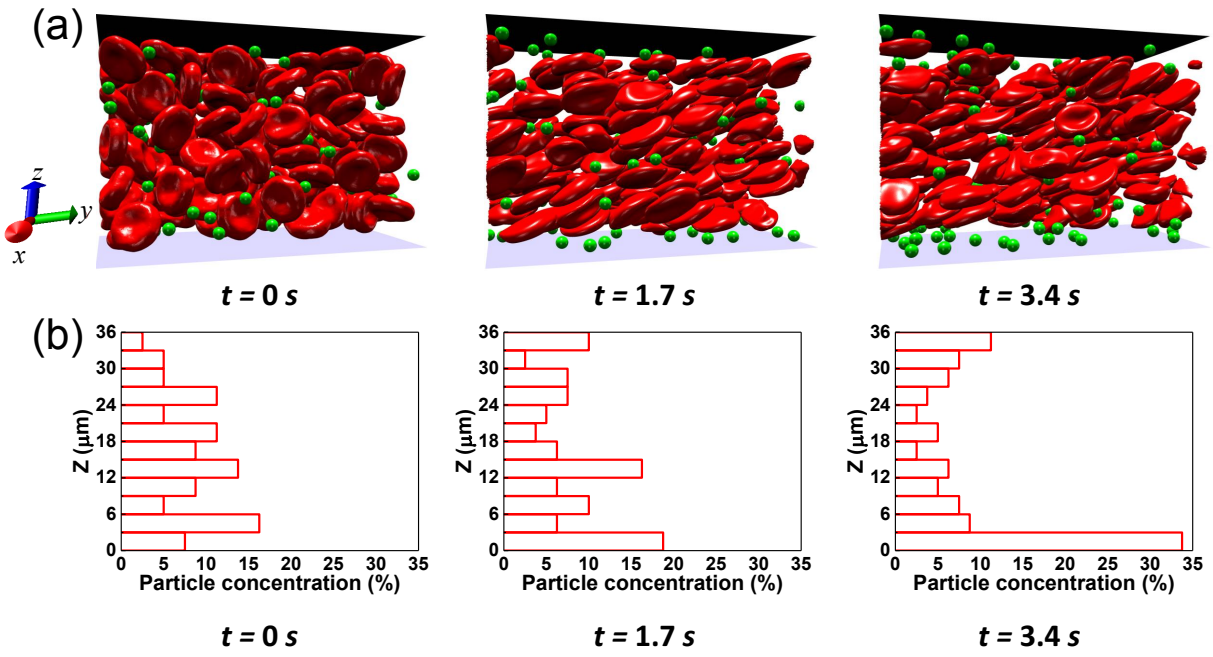

Fig. 12. Margination of spherical MPs under the influence of adhesion. (a) Snapshots for margination behavior of spherical MPs. (b) Distribution of spherical particles along (z)-direction.

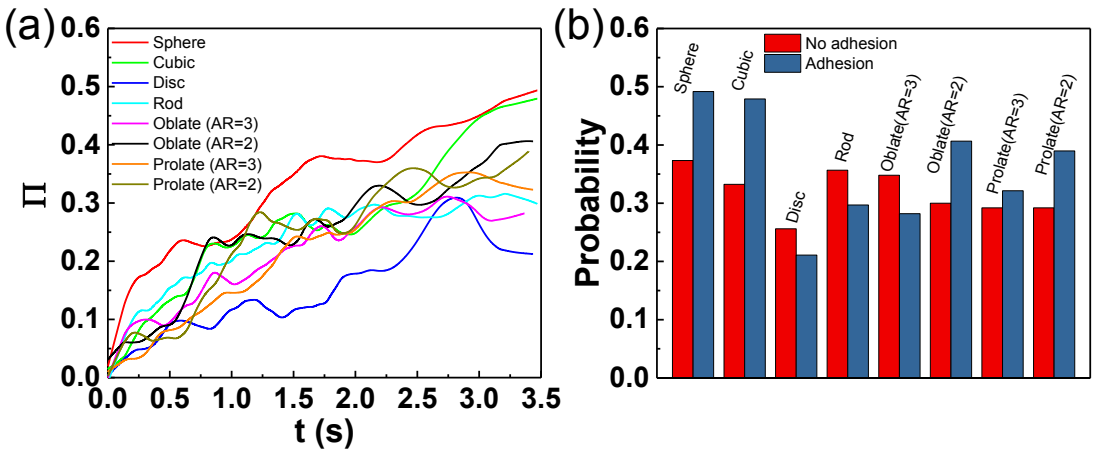

Fig. 13. (a) Evolution of margination probability of different shaped MPs under influence of adhesion. (b) Comparison of margination probabilities between cases with and without adhesion.

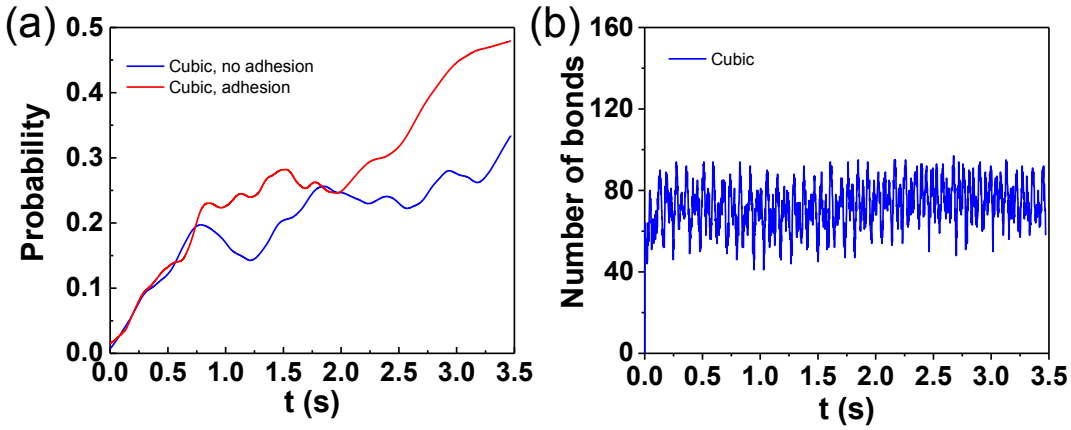

Fig. 14. (a) Margination probabilities of cubic particle with and without adhesion. (b) Number of bonds of a single cubic particle when moving close to substrate.

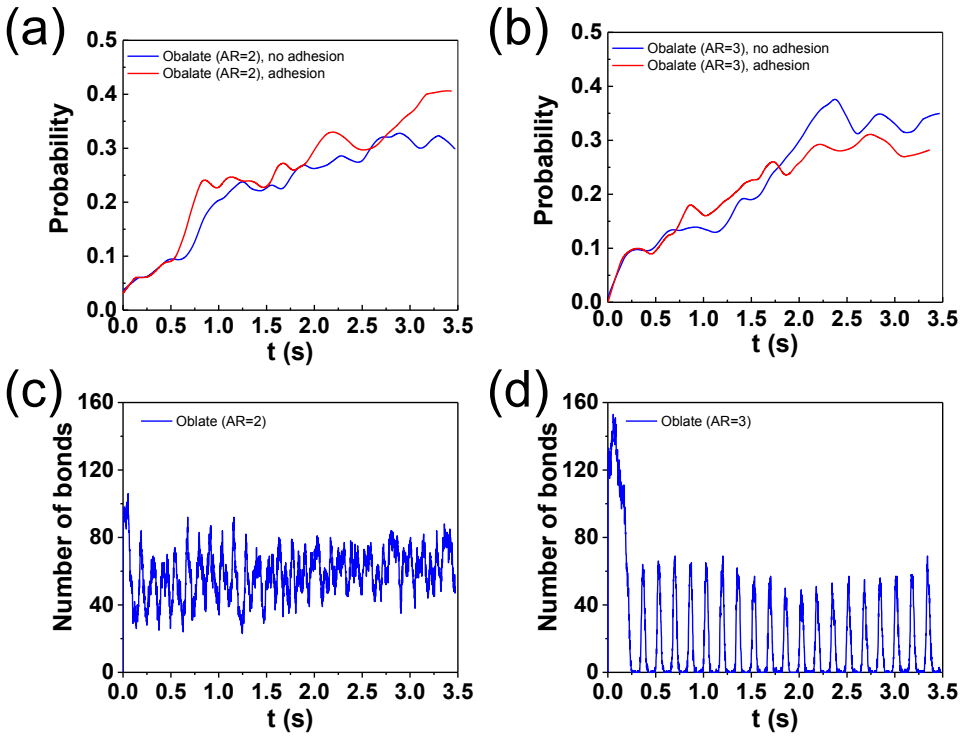

Fig. 15. Margination probabilities of (a) oblate particle with AR=2 and (b) oblate particle with AR=3. Number of bonds for a single (c) oblate particle with AR=2 and (d) oblate particle with AR=3 when moving close to substrate.

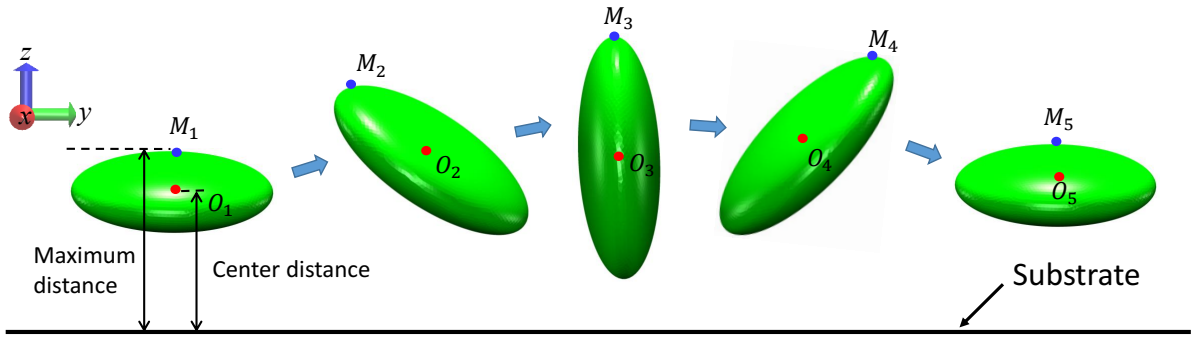

Fig. 16. Snapshots of one tumbling period of oblate particle to show the near substrate motion under adhesion effect. O_1 to O_5 represent the trajectories of particle center, and M_1 to M_5 denote the trajectories of maximum distance between particle and substrate.

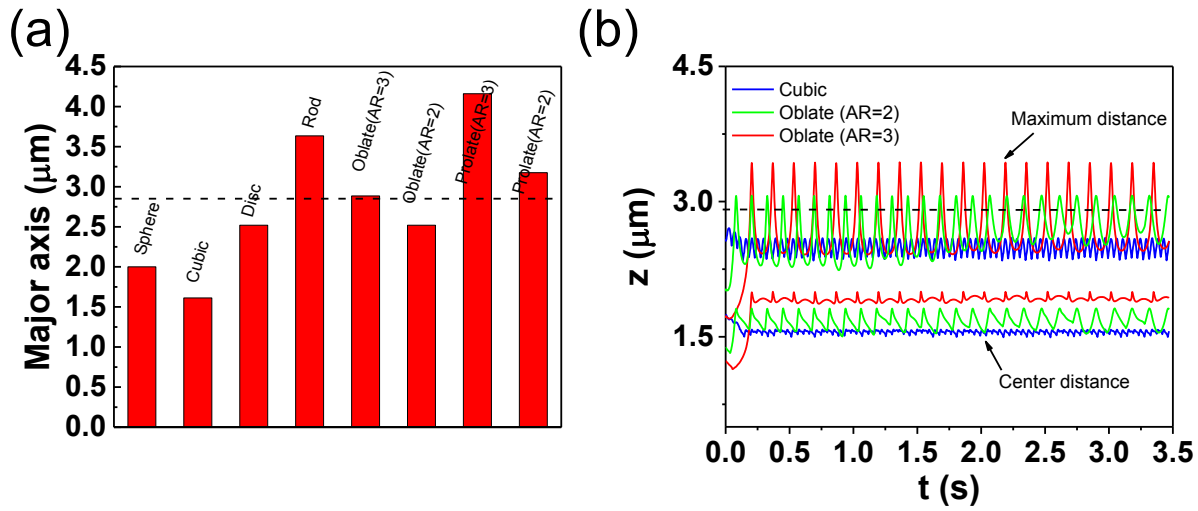

Fig. 17. (a) Distribution of major axes of MPs. Dashed black line shows the thickness of CFL under hematocrit 30 %. (b) Evolution of maximum distance and center for cubic, oblate (AR=2) and oblate (AR=3) MPs.

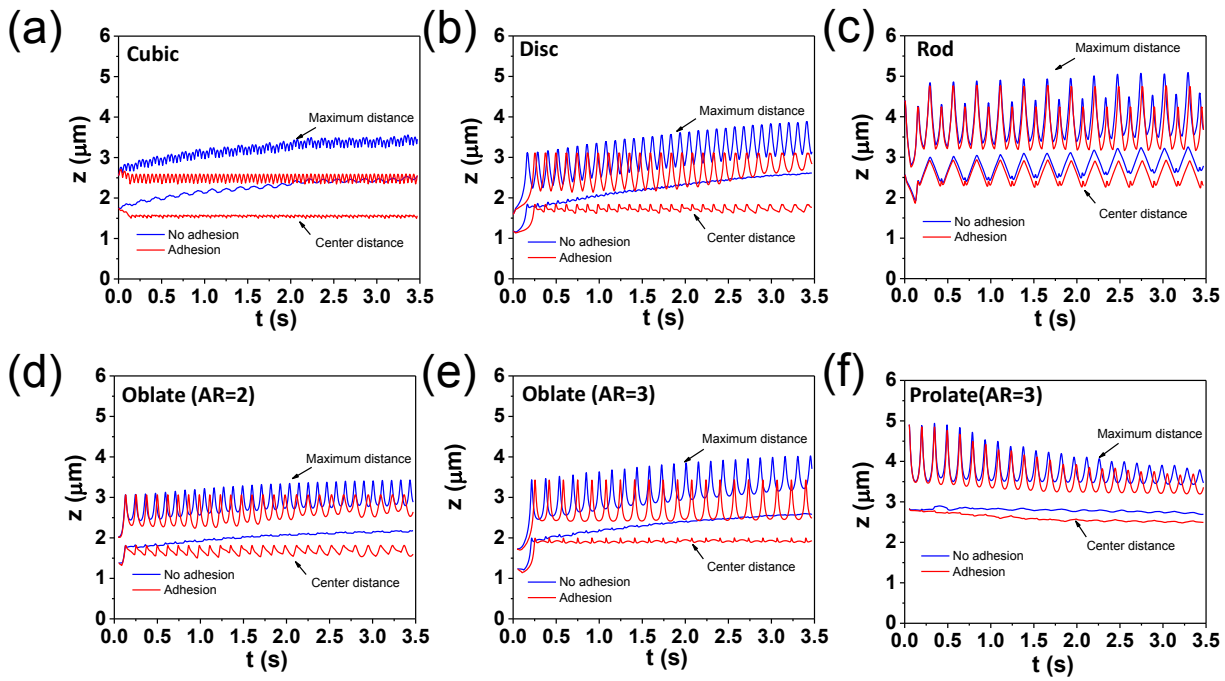

Fig. 18. Comparison of trajectories for maximum distance and center of a single particle motion near substrate with and without adhesion.

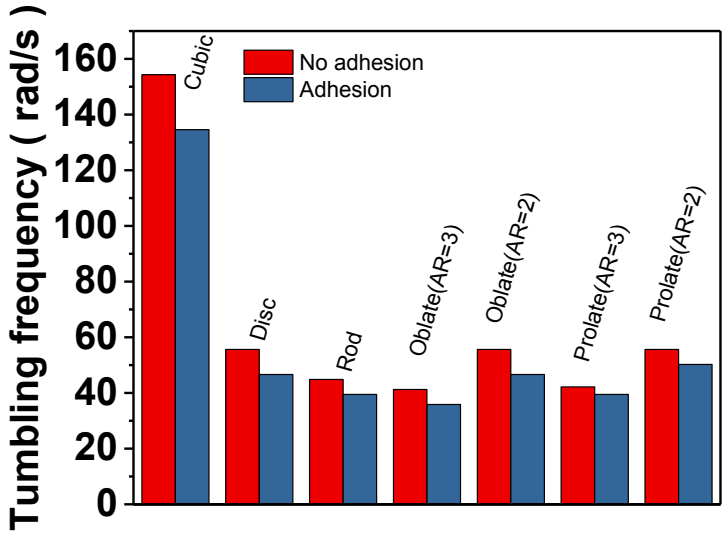

Fig. 19. Comparison of tumbling frequencies of MPs with and without adhesion.

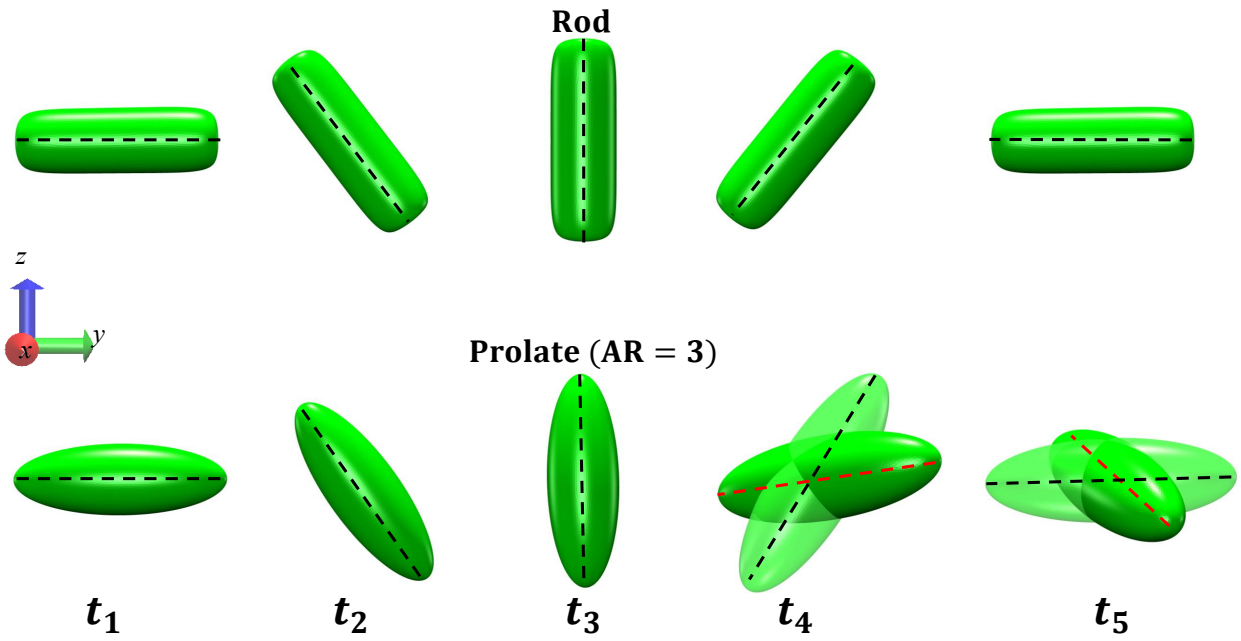

Fig. 20. Comparison of motions of rod and prolate (AR=3) near the substrate. The black dashed lines show the major axes under regular tumbling motion, and the red dashed line denotes the precession of prolate particle.